

1 **Title: Pathogenic *SPTBN1* variants cause a novel autosomal dominant neurodevelopmental syndrome**

2 **Authors:** Margot A. Cousin<sup>1,2\*</sup>, Keith A. Breau<sup>3</sup>, Blake A. Creighton<sup>3</sup>, Rebecca C. Spillmann<sup>4</sup>, Erin Torti<sup>5</sup>,  
3 Sruthi Dontu<sup>3</sup>, Swarnendu Tripathi<sup>6</sup>, Deepa Ajit<sup>3</sup>, Kathryn M. Harper<sup>7,8</sup>, Michael C. Stankewich<sup>9</sup>, Richard E.  
4 Person<sup>5</sup>, Yue Si<sup>5</sup>, Elizabeth A. Normand<sup>5</sup>, Amy Blevins<sup>5</sup>, Alison S. May<sup>10</sup>, Louise Bier<sup>11</sup>, Vimla Aggarwal<sup>11,12</sup>,  
5 Grazia M. S. Mancini<sup>13</sup>, Marjon A. van Slegtenhorst<sup>13</sup>, Kirsten Cremer<sup>14</sup>, Jessica Becker<sup>14</sup>, Hartmut Engels<sup>14</sup>,  
6 Stefan Aretz<sup>14</sup>, Jennifer J. MacKenzie<sup>15</sup>, Eva Brilstra<sup>16</sup>, Koen L. I. van Gassen<sup>16</sup>, Richard H. van Jaarsveld<sup>16</sup>,  
7 Renske Oegema<sup>16</sup>, Gretchen M. Parsons<sup>17</sup>, Paul Mark<sup>17</sup>, Ingo Helbig<sup>18,19</sup>, Sarah E. McKeown<sup>18,19</sup>, Robert  
8 Stratton<sup>20</sup>, Benjamin Cogne<sup>21,22</sup>, Bertrand Isidor<sup>21,22</sup>, Pilar Cacheiro<sup>23</sup>, Damian Smedley<sup>23</sup>, Helen V. Firth<sup>24,25</sup>,  
9 Tatjana Bierhals<sup>26</sup>, Katja Kloth<sup>26</sup>, Deike Weiss<sup>27</sup>, Cecilia Fairley<sup>28,29</sup>, Joseph T. Shieh<sup>28,29</sup>, Amy Kritzer<sup>30</sup>, Parul  
10 Jayakar<sup>31</sup>, Evangeline Kurtz-Nelson<sup>32</sup>, Raphael Bernier<sup>32</sup>, Tianyun Wang<sup>33</sup>, Evan E. Eichler<sup>33,34</sup>, Ingrid M.B.H.  
11 van de Laar<sup>13</sup>, Allyn McConkie-Rosell<sup>4</sup>, Marie McDonald<sup>4</sup>, Jennifer Kemppainen<sup>1,35</sup>, Brendan C. Lanpher<sup>1,35</sup>,  
12 Laura E. Schultz-Rogers<sup>1,2</sup>, Lauren B. Gunderson<sup>1,35</sup>, Pavel N. Pichurin<sup>1</sup>, Grace Yoon<sup>36</sup>, Michael Zech<sup>37,38</sup>,  
13 Robert Jech<sup>39</sup>, Juliane Winkelmann<sup>37,38,40,41</sup>, Undiagnosed Diseases Network<sup>#</sup>, Genomics England Research  
14 Consortium<sup>#</sup>, Michael T. Zimmermann<sup>6,42,43</sup>, Brenda Temple<sup>44</sup>, Sheryl S. Moy<sup>7,8</sup>, Eric W. Klee<sup>1,2,35</sup>, Queenie  
15 K.-G. Tan<sup>4</sup>, Damaris N. Lorenzo<sup>3,8,45\*</sup>

- 16 1. Center for Individualized Medicine, Mayo Clinic, Rochester, MN, USA
- 17 2. Department of Health Sciences Research, Mayo Clinic, Rochester, MN, USA
- 18 3. Department of Cell Biology and Physiology, University of North Carolina at Chapel Hill, Chapel  
19 Hill, NC, USA
- 20 4. Department of Pediatrics, Duke University Medical Center, Duke University, Durham, NC, USA
- 21 5. GeneDx, Gaithersburg, MD, USA
- 22 6. Bioinformatics Research and Development Laboratory, Genomic Sciences and Precision  
23 Medicine Center, Medical College of Wisconsin, Milwaukee, WI, USA

- 24 7. Department of Psychiatry, University of North Carolina at Chapel Hill, Chapel Hill, NC, USA
- 25 8. Carolina Institute for Developmental Disabilities, University of North Carolina at Chapel Hill,  
26 Chapel Hill, NC, USA
- 27 9. Department of Pathology, Yale University, New Haven, CT, USA
- 28 10. Department of Neurology, Columbia University, NY, USA
- 29 11. Institute for Genomic Medicine, Columbia University, NY, USA
- 30 12. Laboratory of Personalized Genomic Medicine, Department of Pathology and Cell Biology,  
31 Columbia University, NY, USA
- 32 13. Department of Clinical Genetics, Erasmus MC University Medical Center, 3015GD Rotterdam,  
33 The Netherlands
- 34 14. Institute of Human Genetics, University of Bonn, School of Medicine & University Hospital Bonn,  
35 Bonn, Germany
- 36 15. McMaster University, Hamilton, ON, Canada
- 37 16. Department of Genetics, University Medical Center Utrecht, Utrecht, The Netherlands
- 38 17. Spectrum Health Medical Genetics, USA
- 39 18. Division of Neurology, Departments of Neurology and Pediatrics, The Children's Hospital of  
40 Philadelphia and the Perelman School of Medicine at the University of Pennsylvania,  
41 Philadelphia, PA, USA
- 42 19. The Epilepsy NeuroGenetics Initiative, Children's Hospital of Philadelphia, Philadelphia, PA, USA
- 43 20. Genetics, Driscoll Children's Hospital, Corpus Christi, TX, USA
- 44 21. Service de Génétique Médicale, CHU Nantes, Nantes, France

- 45        22. Université de Nantes, CNRS, INSERM, L'Institut du Thorax, Nantes, France
- 46        23. William Harvey Research Institute, School of Medicine and Dentistry, Queen Mary University of  
47            London, London, UK.
- 48        24. Cambridge University Hospitals, UK
- 49        25. Wellcome Sanger Institute, Hinxton, UK
- 50        26. Institute of Human Genetics, University Medical Center Hamburg-Eppendorf, Hamburg,  
51            Germany
- 52        27. Department of Pediatrics, Neuropediatrics, University Medical Center Hamburg-Eppendorf,  
53            Hamburg, Germany
- 54        28. Institute for Human Genetics, University of California San Francisco, San Francisco, CA, USA.
- 55        29. Division of Medical Genetics, Department of Pediatrics, University of California San Francisco,  
56            San Francisco, CA, USA.
- 57        30. Boston Children's Hospital, Division of Genetics and Genomics, MA, USA
- 58        31. Nicklaus Children's Hospital, Miami, FL, USA
- 59        32. Department of Psychiatry and Behavioral Sciences, University of Washington, Seattle, WA, USA
- 60        33. Department of Genome Sciences, University of Washington School of Medicine, Seattle, WA,  
61            USA
- 62        34. Howard Hughes Medical Institute, Seattle, WA, USA
- 63        35. Department of Clinical Genomics, Mayo Clinic, Rochester, MN, USA
- 64        36. Divisions of Clinical/Metabolic Genetics and Neurology, The Hospital for Sick Children, University  
65            of Toronto, Toronto, Canada

- 66 37. Institute of Neurogenomics, Helmholtz Zentrum München, Munich, Germany
- 67 38. Institute of Human Genetics, Technical University of Munich, Munich, Germany
- 68 39. Department of Neurology, Charles University, 1<sup>st</sup> Faculty of Medicine and General University  
69 Hospital in Prague, Prague, Czech Republic
- 70 40. Lehrstuhl für Neurogenetik, Technische Universität München, Munich, Germany
- 71 41. Munich Cluster for Systems Neurology, SyNergy, Munich, Germany
- 72 42. Department of Biochemistry, Medical College of Wisconsin, Milwaukee, WI, USA
- 73 43. Clinical and Translational Sciences Institute, Medical College of Wisconsin, Milwaukee, WI, USA
- 74 44. Department of Biochemistry, University of North Carolina at Chapel Hill, Chapel Hill, NC, USA
- 75 45. Neuroscience Center, University of North Carolina at Chapel Hill, Chapel Hill, NC, USA

76

77 \*Corresponding author

78 #A complete list of consortia members is provided in the Supplementary Note

79

80

81

82

83

84

85

86 **Abstract**

87 *SPTBN1* encodes  $\beta$ II-spectrin, the ubiquitously expressed member of the  $\beta$ -spectrin family that forms  
88 micrometer-scale networks associated with plasma membranes.  $\beta$ II-spectrin is abundantly expressed in  
89 the brain, where it is essential for neuronal development and connectivity. Mice deficient in neuronal  $\beta$ II-  
90 spectrin expression have defects in cortical organization, global developmental delay, dysmorphisms, and  
91 behavioral deficiencies of corresponding severity. These phenotypes, while less severe, are observed in  
92 haploinsufficient animals, suggesting that individuals carrying heterozygous variants in this gene may also  
93 present with measurable compromise of neural development and function. Here we report the  
94 identification of heterozygous *SPTBN1* variants in 29 individuals who present with global developmental,  
95 language and motor delays, mild to severe intellectual disability, autistic features, seizures, behavioral  
96 and movement abnormalities, hypotonia, and variable dysmorphic facial features. We show that  
97 these *SPTBN1* variants lead to loss-of-function, gain-of-function, and dominant negative effects that  
98 affect protein stability, disrupt binding to key protein partners, and disturb cytoskeleton organization and  
99 dynamics. Our studies define the genetic basis of this new neurodevelopmental syndrome, expand the  
100 set of spectrinopathies affecting the brain and neural development, and underscore the critical role of  $\beta$ II-  
101 spectrin in the central nervous system.

102

103

104

105

106

107

## 108 Introduction

109 Spectrins are ubiquitously expressed, elongated polypeptides that bind membrane lipids and ankyrins to  
110 line the plasma membrane<sup>1,2</sup>. The spectrin meshwork is formed by heterodimeric units of  $\alpha$ - and  $\beta$ -  
111 spectrin assembled side-to-side in antiparallel fashion, which then form head-to-head tetramers that  
112 crosslink F-actin to form spectrin-actin arrays<sup>1,2</sup>. Mammalian neurons express the most diverse repertoire  
113 of spectrins ( $\alpha$ II- and  $\beta$ I-V spectrins) of any cell type<sup>3</sup>. Together with ankyrins, spectrins self-assemble with  
114 both remarkable long-range regularity and micro- and nanoscale specificity to precisely position and  
115 stabilize cell adhesion molecules, membrane transporters, ion channels, and other cytoskeletal proteins<sup>3</sup>.  
116 Some spectrins also enable intracellular organelle transport<sup>3</sup>. Unsurprisingly, deficits in spectrins underlie  
117 several neurodevelopmental and neurodegenerative disorders<sup>4-6</sup>. For example, inherited autosomal  
118 dominant variants in  $\beta$ III-spectrin (encoded by *SPTBN2*) cause late onset spinocerebellar ataxia type 5  
119 (SCA5)<sup>5</sup>, while pathogenic *de novo* variants have been associated with early childhood ataxia, intellectual  
120 disability (ID), and developmental delay (DD)<sup>7-12</sup>. Similarly, autosomal recessive *SPTBN2* variants<sup>13-15</sup> are  
121 associated with childhood ataxia, which may also present with ID and DD<sup>13</sup>, collectively referred to as  
122 autosomal recessive spinocerebellar ataxia 14 (SCAR14). *De novo* pathogenic variants in *SPTAN1*, which  
123 encodes  $\alpha$ II-spectrin, cause West syndrome, an early-infantile epileptic encephalopathy (EIEE)  
124 characterized by frequent severe seizures and persistent abnormality of cortical function<sup>5</sup>, and other  
125 childhood onset epileptic syndromes<sup>16-20</sup>. Some patients co-present with spastic quadriplegia, DD, and  
126 various brain defects<sup>5</sup>. In addition, dominantly inherited *SPTAN1* nonsense variants were recently linked  
127 to juvenile onset hereditary motor neuropathy<sup>21</sup>. Biallelic alterations in  $\beta$ IV-spectrin (encoded by *SPTBN4*)  
128 result in congenital hypotonia, neuropathy, and deafness, with and without ID<sup>6,22,23</sup>.

129 Neuronal  $\beta$ II-spectrin, encoded by *SPTBN1*, is the most abundant  $\beta$ -spectrin in the brain and forms  
130 tetramers with  $\alpha$ II-spectrin, which intercalate F-actin rings to build a sub-membranous periodic skeleton  
131 (MPS)<sup>24</sup>. A cytosolic pool of  $\beta$ II-spectrin promotes bidirectional axonal organelle transport<sup>25,26</sup>. We

132 previously reported that mice lacking  $\beta$ II-spectrin in all neural progenitors (*Sptbn1*<sup>flox/flox</sup>;Nestin-Cre;  
133 referred to as  $\beta$ IIsp-KO) show early postnatal lethality, reduced long-range cortical and cerebellar  
134 connectivity, spontaneous seizures, and motor deficits<sup>26</sup>. However, the impact of human genetic variation  
135 in *SPTBN1* on  $\beta$ II-spectrin function and its association with disease has not been studied. Here we describe  
136 a cohort of 29 individuals carrying rare, mostly *de novo* variants in *SPTBN1* affected by a novel autosomal  
137 dominant neurologic syndrome presenting with global developmental, language and motor delays, mild  
138 to severe ID, autistic features, seizures, behavioral abnormalities, hypotonia, and variable dysmorphisms.  
139 This suggests conserved roles for  $\beta$ II-spectrin in neuronal development and function. The most damaging  
140 variants clustered within the actin-binding calponin homology domain (CH) and led to aberrant neuronal  
141 morphology, decreased neurite outgrowth, and deficient axonal organelle transport in primary neurons.  
142 Consistent with these deficiencies, our biochemistry, microscopy, and molecular modeling studies  
143 indicate that *SPTBN1* variants lead to loss-of-function (LOF), gain-of-function (GOF), and dominant  
144 negative effects that affect protein stability, disrupt binding to key protein partners, and affect  
145 cytoskeleton organization and dynamics. Consequently, histology and behavioral studies in brain  $\beta$ II-  
146 spectrin-deficient mice showed neuron-autonomous brain connectivity defects and recapitulated  
147 developmental and behavioral phenotypes observed in patients with *SPTBN1* variants. Collectively, our  
148 data strongly support pathogenic mechanisms of *SPTBN1* variants as the genetic cause of a novel  
149 neurodevelopmental syndrome and underscores the multifaceted role of  $\beta$ II-spectrin in the nervous  
150 system.

## 151 **Results**

### 152 **Patients with *SPTBN1* variants present with a novel neurodevelopmental syndrome**

153 A cohort of 29 individuals from 28 families (one pair of siblings) who carry heterozygous variants in *SPTBN1*  
154 was identified through whole genome (WGS) or exome (WES) sequencing. These probands presented with

155 neurodevelopmental delay and variable neurologic, behavioral, and dysmorphic features (Fig. 1, Table 1,  
156 Supplementary Note). Twenty-four of the 29 affected individuals carry *de novo* variants, while the  
157 remaining have unknown inheritance due to lack of parental samples for testing (Supplementary Table 1).  
158 In proband P17 the *SPTBN1* variant inheritance was unknown but sequencing revealed mosaicism at  
159 13.3% of reads suggesting the variant occurred *de novo*. Twenty-eight unique variants are described (P10  
160 has two *de novo* variants in cis) of which 22 are missense, three are nonsense, and three are canonical  
161 splice-site variants, with two predicted by SpliceAI<sup>27</sup> to lead to in-frame deletions and one predicted to  
162 result in a frameshift that introduces a premature stop codon (Fig. 1a, Supplementary Table 1).  
163 Approximately half of the variants cluster in the CH domain, predominantly in the second CH domain  
164 (CH2), with the rest distributed in various spectrin repeats (SR) (Fig. 1a).

165 The phenotypic findings are summarized in Table 1 and detailed clinical and family histories are included  
166 in the Supplementary Note. The cohort included 17 male and 12 female probands with the age at last  
167 evaluation spanning from 6 months to 26 years of age. All had early onset of symptoms with primarily  
168 developmental delay (DD) presentations with the exception of two individuals. For 28 individuals with  
169 phenotypic data, 26 reported some level of delays. Of those with DD, 21 reported both speech (SD) and  
170 motor (MD) delays, three reported only SD (P16, P26 and P27), and one reported only MD (P29). Twenty  
171 individuals reported ID, with seven of those being severe or moderate to severe, and six being mild or low  
172 to normal. Developmental regression was noted in three individuals. Although mild delays were noted in  
173 the clinical evaluation of proband P29 (c.5961+2T>C, p.(I1988Afs\*90)), the primary symptom, dystonia,  
174 was observed at age 13. Similarly, while delay in speaking was noted for proband P23 (p.A1086T), the  
175 primary phenotype in this individual was liver-related. Only partial phenotype information was obtained  
176 for previously reported probands P4 and P25<sup>28</sup>, and no specific phenotypic information is available for P3  
177 from the Deciphering Developmental Disorders (DECIPHER) database<sup>29</sup>, although this individual was  
178 presumed to have some form of DD (Supplementary Note).

179 Nine individuals have a history of seizures, with two being febrile only, and six with electroencephalogram  
180 (EEG) correlates. Seizure episodes in four of the cases were resolved later in childhood or were  
181 successfully managed through medication. Four of these patients were diagnosed with frontal lobe or  
182 generalized epilepsy. Seven individuals had abnormal brain MRI findings, including three patients with  
183 thinning of the corpus callosum (CC), two with ventriculomegaly, two with delayed myelination, and two  
184 showing some volume loss (P1: diffuse cerebral parenchymal; P10: mild cerebellar and vermian). The  
185 remaining brain MRI findings were unique (Table 1, Supplementary Note). Behavioral concerns were  
186 common within the cohort. Six individuals displayed autistic features or had an autism spectrum disorder  
187 (ASD) diagnosis, including two (P19 and P24) previously reported as part of a WES study of a 2,500 ASD  
188 patient cohort<sup>30</sup>. One other proband (P25) was originally identified as part of a WES study of over 500 trios  
189 from Tourette syndrome cohorts<sup>28</sup>. Thirteen individuals presented with other behavioral concerns,  
190 including attention deficit and hyperactivity disorder (ADD/ADHD) (n=11), anxiety (n=3), emotional  
191 lability including tantrums and depression (n=7), and aggressive or self-injurious behaviors (n=6). Seven  
192 individuals experienced sleep disturbances, in some cases co-occurring with seizure episodes. Additional  
193 phenotypic findings include changes in muscle tone and movement abnormalities. Ten had hyper- (n=4)  
194 or hypotonia (n=8). Seven individuals reported movement abnormalities including dystonia (n=3), ataxic  
195 or unsteady gait (n=5), spasticity (n=1), and tremor (n=2). Less common features included hearing  
196 impairment, reported for five individuals, generally mild to moderate, with one individual suspected to  
197 have conductive hearing loss due to recurrent ear infections. Dysmorphic features were noted in 18  
198 individuals with a subset of individuals shown in Fig. 1c, but no consistent findings were observed.  
199 Macrocephaly (n=5) and microcephaly (n=5) were both observed as well as other head shape anomalies  
200 (n=6).

201 *SPTBN1* is intolerant to both missense and loss-of-function variants (gnomAD v2.1.1)<sup>31</sup>, and protein  
202 sequence alignment of human  $\beta$ II-spectrin and its orthologues across several species shows a high degree

203 of evolutionary conservation of the residues impacted by these putative pathogenic variants (Fig. 1b).  
204 Consistent with their implied functional relevance, the majority of the variants are predicted to be likely  
205 damaging to protein function by multiple prediction tools (PolyPhen-2, Mutation Taster, SIFT, PROVEAN,  
206 M-CAP, PredictSNP2, and CADD) (Supplementary Table 1). Additionally, all variants are absent or  
207 extremely rare in the population (gnomAD v2.1.1)<sup>31</sup> (Supplementary Table 1). Missense variants in codons  
208 G205, T268, R411 and R1003 were identified in more than one individual (Fig. 1a). The p.R1003W variant  
209 was identified in two maternal half-siblings (P21 and P22) inherited from their unaffected mother, who  
210 was found to be mosaic for the variant at a low level (found in 1.8% of next generation sequencing reads).  
211 Unrelated individual P20 also carries the *de novo* p.R1003W variant, and has the common DD features,  
212 but also presented with some non-overlapping clinical features. Similarly, variants in unrelated duos P4  
213 and P5, and P15 and P16 affect the same p.G205 and p.R411 residues, respectively, but result in different  
214 amino acid substitutions. All of these individuals have DD, both P4 and P5 had an abnormal EEG, and both  
215 P15 and P16 had hypotonia but each also has some distinct features consistent with the variability in the  
216 cohort. Likewise, unrelated patients P10, P11, and P12 carry different amino acid substitutions in residue  
217 p.T268, and present with overlapping phenotypes. Notably, P10 has two  $\beta$ II-spectrin variants *in cis*  
218 (p.F344L and p.T268A), which may contribute to the more severe phenotype observed. The partial clinical  
219 divergence within these patients likely stems from differences in sex, age, and genomic background, which  
220 in turn may determine their corresponding penetrance and physiological consequences.

221 In sum, the above clinical presentations suggest that *SPTBN1* variants converge to impair cellular and  
222 physiological mechanisms that lead to delays in motor and language development and cognitive skills.  
223 Additionally, the results of these evaluations suggest that several of these variants also result in additional  
224 neurological and behavioral phenotypes. These observations are consistent with pleiotropic functions of  
225  $\beta$ II-spectrin including its diverse and critical roles in brain development and function<sup>26</sup>.

226 **Human  $\beta$ II-spectrin mutations affect protein cellular distribution and alter cell morphology**

227 To begin to assess the pathogenic mechanisms of *SPTBN1* variants, we introduced a subset of the  
228 mutations in the coding sequence of human  $\beta$ II-spectrin cloned into the peGFP-C3 plasmid, transfected  
229 the constructs into HEK293 cells, either alone or together with pmCherry-C1, and monitored their effects  
230 on GFP- $\beta$ II-spectrin (GFP- $\beta$ IISp) levels, localization, size, and stability by confocal microscopy and western  
231 blot. Of the 22 mutations tested, protein levels, of 10 were unchanged relative to control (Fig. 2a,  
232 Extended Data Fig. 1a). Variants p.H275R and p.A850G resulted in 25% and 50%  $\beta$ II-spectrin  
233 overexpression, respectively. Expression of nonsense p.C183\*, p.E892\* and p.W1787\* variants yielded  
234 truncated proteins of the expected size. However, while p.W1787\* was expressed normally, the levels of  
235 the p.C183\* and p.E892\* mutants were significantly reduced. While neither of the two CH domain in-  
236 frame deletions (I159\_Q160del and Y190\_R216del) affected protein levels, several mutations in this  
237 region showed lower expression. Both p.G205D and p.G205S mutations reduced protein levels, with  
238 p.G205D also impacting  $\beta$ II-spectrin solubility, which largely precipitated into the Triton-X100 insoluble  
239 fraction (Fig. 2b, Extended Data Fig. 1b). This indicates that these amino acid substitutions at p.G205 likely  
240 affect the structural conformation of  $\beta$ II-spectrin, and result in unfolded and unstable polypeptides.  
241 Notably, wildtype (WT) GFP- $\beta$ IISp localized through the cytosol and at the cell membrane whereas GFP-  
242  $\beta$ IISp bearing p.I159\_Q160del at the end of CH1, or the p.C183\*, p.Y190\_R216del, p.G205D, and p.G205S  
243 mutations in the proximal CH2 domain accumulated in large cytosolic aggregates (white arrowheads Fig.  
244 2c and Extended Data Fig. 1c). Expression of the CH2 mutations p.T268A, T268N, T268S, V271M, and  
245 H275R resulted in normal GFP- $\beta$ IISp distribution, but induced noticeable changes in cell morphology.  
246 Overall, cells were enlarged and had increased membrane protrusions (Fig. 2c and Extended Data Fig. 1c,  
247 asterisks). These changes are indicative of modified cytoskeleton arrangements and dynamics, and likely  
248 reflect altered F-actin binding.

249 Cell morphology phenotypes induced by SR mutations varied. For example, cells expressing the p.R411W  
250 mutation, located in SR1, which is required for dimerization with  $\alpha$ II-spectrin<sup>32</sup> and thought to contribute

251 to actin binding<sup>33</sup>, were enlarged and with increased membrane protrusions. Among the five mutations  
252 clustered within SR6-8, p.A850G and p.R1003W induced the most noticeable morphological changes (Fig.  
253 2c, Extended Data Fig. 1c). Interestingly, p.A850G, which results in  $\beta$ II-spectrin overexpression, also causes  
254 a striking increase in membrane protrusions, which suggests a GOF effect (Fig. 2c and Extended Data Fig.  
255 1c). Since SR3-S14 have no assigned functional specificity nor contain known binding sites for partners, a  
256 molecular rationale for how mutations in this region affect  $\beta$ II-spectrin function is lacking. SR15 binds  
257 ankyrins, with amino acid p.Y1874 known to be critical for this interaction<sup>34</sup>. However, p.E1886Q GFP-  
258  $\beta$ IISp does not show apparent cellular changes, likely because it does not disrupt binding to ankyrins<sup>34</sup>, or  
259 this complex is not required for cytoskeleton organization or dynamics in HEK293 cells. Expression of  
260 E892\* and W1787\* GFP- $\beta$ IISp, lacking the polypeptide portions from SR6 to C-terminus and SR14 to C-  
261 terminus respectively, did not cause apparent cellular phenotypes. This is surprising because in addition  
262 to loss of ankyrin binding, these truncated proteins also lack the tetramerization<sup>35</sup> and pleckstrin  
263 homology (PH) domains<sup>36</sup>, the latter being important for binding lipids in the cell and organelle  
264 membranes. Together, these data indicate that human  $\beta$ II-spectrin mutations can lead to cellular  
265 phenotypes through LOF and GOF mechanisms that likely involve changes in cytoskeleton architecture  
266 and dynamics.

### 267 **Human $\beta$ II-spectrin mutations affect its interaction with submembrane cytoskeleton partners**

268 A subcortical network of F-actin- and ankyrin-bound  $\beta$ II-/ $\alpha$ II-spectrin tetramers promotes membrane  
269 stability and helps organizing membrane proteins within specialized microdomains<sup>1-3</sup>. Thus, pathogenic  
270 *SPTBN1* variants could impair neuronal development and/or function by altering  $\beta$ II-spectrin interaction  
271 with F-actin and other cytoskeletal partners or their submembrane availability. Consistent with the latter  
272 prediction, we found that both actin and mCherry- $\alpha$ IISp were sequestered in GFP- $\beta$ IISp aggregates caused  
273 by expression of various CH domain variants in HEK293 cells (arrowheads, Fig. 3a, Extended Data Fig. 2a).  
274 These mutations in the CH domain (F-actin binding region) also resulted in GFP- $\beta$ IISp aggregation and in

275 clustering of endogenous actin and  $\alpha$ II-spectrin within GFP aggregates when expressed in cortical neurons  
276 from  $\beta$ II-SpKO mice (arrowheads, Fig. 3b). To further evaluate the ability of mutant  $\beta$ II-spectrin to  
277 associate with molecular partners, we conducted binding assays and co-immunoprecipitation (co-IP)  
278 experiments. We prioritized the evaluation of a subset of variants based on the likelihood that they would  
279 have an effect on the interaction tested, given their position on the specific domains known to be critical  
280 for binding to that specific partner. We first assessed the effect of the mutations on the formation of  $\beta$ II-  
281 spectrin/ $\alpha$ II-spectrin complexes by incubating GFP beads coupled to WT or mutant GFP- $\beta$ II Sp with cell  
282 lysates expressing mCherry- $\alpha$ II Sp and measuring the amount of mCherry- $\alpha$ II Sp in eluates from GFP  
283 pull-downs by western blot. As expected, mutant C183\* GFP- $\beta$ II Sp neither associated with mCherry- $\alpha$ II Sp  
284 in pull-down assays nor sequestered mCherry- $\alpha$ II Sp or endogenous  $\alpha$ II-spectrin into GFP- $\beta$ II Sp aggregates  
285 in HEK293 or neurons because it lacks the heterodimer nucleation SR1-SR2 region<sup>30</sup> (Fig. 3a-c and  
286 Extended Data Fig. 2b). Similarly, the pull-down of  $\alpha$ II-spectrin with G205D and G205S GFP- $\beta$ II Sp baits  
287 yielded less  $\alpha$ II-/ $\beta$ II-spectrin complexes, partly due to the lower expression of these mutant polypeptides,  
288 but it also indicates a lower affinity for  $\alpha$ II-spectrin (Fig. 3a-c and Extended Data Fig. 2b). That a single  
289 substitution in CH2 reduces  $\alpha$ II-spectrin affinity is surprising because this domain has not been linked to  
290  $\alpha$ II-spectrin binding. With the exception of the p.R1003W mutant located in SR7, which reduces  
291 association with  $\alpha$ II-spectrin by 40%, none of the other variants tested affects  $\alpha$ II-spectrin binding (Fig. 3c  
292 and Extended Data Fig. 2a, b). The lower  $\alpha$ II-spectrin binding to R1003W GFP- $\beta$ II Sp might result from local  
293 or long-range conformational changes that weakens interactions along the dimer.

294 Next, we evaluated whether mutations in the CH domains, the known actin-binding domain in  $\beta$ II-spectrin,  
295 affect its binding to F-actin using a co-sedimentation assay.  $\beta$ II-spectrin proteins containing a PreScission  
296 protease (PP) recognition site between GFP and the initiation codon of  $\beta$ II-spectrin (GFP-PP- $\beta$ II Sp) were  
297 produced in HEK293 cells and captured on GFP beads. Purified WT and mutant  $\beta$ II-spectrin were recovered  
298 from beads upon PP cleavage and mixed with purified F-actin. The partition of  $\beta$ II-spectrin between the

299 soluble (S) and actin-containing pellet (P) fractions was used to estimate the relative binding proclivity  
300 between both proteins. We found that CH1 mutation p.T59I and deletion p.I159\_Q160del in the CH1-CH2  
301 linker led to approximately 40% and 70% less  $\beta$ II-spectrin association with F-actin, respectively (Fig. 3d  
302 and Extended Data Fig. 2c). Similarly, p.Y190\_R216del and p.D255E CH2 variants also resulted in reduced  
303 F-actin binding. In contrast, the p.V271M and p.H275R mutations increased F-actin binding to  $\beta$ II-spectrin  
304 by 60-90%, while all three p.T268S/N/A mutants bound F-actin at similar levels as the WT protein (Fig. 3d  
305 and Extended Data Fig. 2c). This range in binding affinity is likely caused by the balance of individual or  
306 combined effects of both local and CH domain-wide conformational changes caused by modified  
307 intramolecular interactions, which in turn results in modified intermolecular contacts at the  $\beta$ II-spectrin/F-  
308 actin interface. Given that the p.A850G mutant causes a cell morphology phenotype similar to the ones  
309 induced by some of the CH domain mutants (Fig. 2c and Extended Data Fig. 1c), we also tested its binding  
310 to F-actin. Surprisingly, this mutant resulted in approximately 50% higher F-actin binding (Fig. 3d and  
311 Extended Data Fig. 2c). While this higher propensity for actin binding is likely to underlie the abnormal cell  
312 morphology, it is not clear how this substitution, several SR away from the CH domain, can modify this  
313 interaction.

314 Finally, we evaluated the impact of  $\beta$ II-spectrin mutations on its interaction with ankyrins. In this  
315 experiment, HA-tagged 220kDa ankyrin-B was expressed in HEK293 cells together with WT or mutant GFP-  
316  $\beta$ II<sub>Sp</sub> proteins. The presence of HA signal in eluates from GFP- $\beta$ II<sub>Sp</sub> complexes was detected by western  
317 blot. Consistent with previous reports<sup>34</sup>, expression of the Y1874 mutation in SR15 (the known ankyrin-  
318 binding domain) almost entirely abrogated binding to ankyrin-B (Fig. 3e and Extended Data Fig. 2d). As  
319 expected, truncated  $\beta$ II-spectrin polypeptides that lack SR15 caused by p.E892\* and p.W1787\* variants  
320 also disrupted binding between these partners (Fig. 3e and Extended Data Fig. 2d). Interestingly, the SR15  
321 p.E1886Q variant did not affect binding to ankyrin-B, despite its spatial proximity to the Y1874 binding  
322 site<sup>34</sup>.

### 323 **Molecular modeling predicts effects of $\beta$ II-spectrin variants on protein stability and F-actin binding**

324 We further assessed the impact of *SPTNB1* variants through molecular modelling. We first modeled the  
325 10 missense variants involving seven residues in the  $\beta$ II-spectrin CH1-CH2 domain. The CH domain is a  
326 protein module of around 100 residues composed of four alpha helices<sup>37</sup> found in cytoskeletal and signal  
327 transduction actin-binding proteins (ABP)<sup>38</sup>. Multiple biochemical studies using ABP containing CH1-CH2  
328 domains, such as spectrin superfamily members  $\alpha$ -actinin-4 (*ACTN4*) and utrophin (*UTRN*), suggest  
329 dynamic transitions between “closed” and “open” configurations of the tandem domains, whereas the  
330 open state is thought to expose CH1 residues to enable its predominant role of binding actin, with CH2  
331 regulating the conformational state through autoinhibition<sup>38</sup>. The electrostatic surface profile of  $\beta$ II-  
332 spectrin CH1 and CH2 domains modeled using an available crystal structure of utrophin<sup>39</sup> indicates that  
333 they each have one electrically active side complementary to each other and one neutral side, consistent  
334 with an energetically balanced closed conformation (Fig. 4a-c). This model also indicates that six of the  
335 eight mutated CH domain residues reside at the CH1-CH2 dimer interface, potentially impacting  
336 interdomain helix-helix interactions, thereby dysregulating the natural autoinhibition (Fig. 4b,c).

337 To refine our prediction of the closed conformation of the  $\beta$ II-spectrin CH1-CH2 domain and to identify  
338 interactions at the interface, we docked the CH2 domain (residues 173-278) of  $\beta$ II-spectrin<sup>40</sup> onto the  
339 available modeled structure of the CH1 domain (residues 55-158) of  $\beta$ III-spectrin (95% homologous with  
340  $\beta$ II-spectrin)<sup>41</sup> and chose the top docking pose (Fig. 4d). This pose was also the same pose compared to  
341 the actinin-4 (PDB ID 6oa6) (unpublished) and utrophin (PDB ID 1qag)<sup>39</sup> closed conformations (Extended  
342 Data Fig. 3a-c). Figure 4i summarizes the key predicted interacting residues at the CH1-CH2 interface and  
343 the structural consequences of the variants in those domains. Four of the eight residues affected by  
344 *SPTNB1* missense variants (T59 in CH1, and L250, T268, and H275 in CH2) are predicted to be involved in  
345 interdomain interactions (Fig. 4d,i). The *SPTNB1* missense variants in these and the two other interface  
346 residues (D255 and V271) are predicted to introduce destabilizing effects (Fig. 4i). For example,

347 substitutions of T268 by Ala (smaller and more hydrophobic), Ser (loss of methyl group), and Asn (larger  
348 and more hydrophilic) likely have different degrees of alteration of the original T268 hydrophobic  
349 interaction with L155 in CH1 and I159 in the CH1-CH2 linker. However, if these amino acid changes in T268  
350 affect the CH1-CH2 domain conformation, they do not result in appreciable changes in F-actin binding  
351 (Fig. 3d and Extended Data Fig. 2c), despite their marked cellular (Fig. 2c, Extended Data Fig. 1c) and  
352 disease-linked effects. Similarly, substitution of glutamic for aspartic acid in D255E is a relatively small  
353 change that does not result in changes in F-actin affinity. On the other hand, both the V271M (larger and  
354 hydrophobic) and the H275R (longer and significantly more hydrophilic) substitutions may impair CH1  
355 binding to cause a shift toward the open CH1-CH2 conformation and higher F-actin affinity. This is also  
356 likely the case for the L250R mutation, which is expected to cause significant steric hindrance by the  
357 clashing of the large, charged residue with a hydrophobic CH1 pocket (Fig. 4e). The molecular and cellular  
358 consequences of this variant remain to be assessed. Conversely, the T59I mutation introduces a slightly  
359 longer, but more hydrophobic group that might promote a stronger interaction with L250 in CH2,  
360 potentially shifting the equilibrium to a CH1-CH2 closed configuration consistent with less F-actin binding  
361 (Fig. 3d and Extended Data Fig. 2c).

362 The amino acid substitutions in the two CH2 sites in the interior of the domain (G205S/D and L247H) are  
363 predicted to cause significant steric hindrance, which likely results in CH2 domain instability (Fig. 4f-h).  
364 G205S/D introduces destabilization by positioning a negative charge on the interior and steric hindrance  
365 against the neighbor N233 and L234 sidechains (Fig. 4g,h), which likely underlies the aggregation of the  
366 mutant protein in cells (Figs. 2c and 3b). The Y190\_R216del mutation, which eliminates 27 amino acids in  
367 the CH2 domain, also results in  $\beta$ II-spectrin aggregation and diminished F-actin binding (Figs. 2c and 3b,d  
368 and Extended Data Fig. 2c). In these cases, the autoinhibitory interactions will also be lost if the structure  
369 of the CH2 domain is compromised, but through a different mechanism than the genetic variants that  
370 alter the CH dimer interface. Besides the open/closed CH1-CH2 domain conformational shifts, some of

371 these mutants might be directly involved in binding F-actin. To explore this possibility, we independently  
372 docked the CH1 and CH2 domains onto an F-actin model built from chains A-F of 6anu<sup>40</sup> using ClusPro<sup>42,43</sup>  
373 (Extended Data Fig. 3d-f). The top eight CH1 docking poses predicted by the balanced and electrostatic  
374 scoring algorithms almost all correspond to the location and orientation of CH1 molecules on F-actin as  
375 defined by the cryo-EM structure 6anu (Extended Data Fig. 3d, dark blue). For CH2 docking onto F-actin,  
376 the top eight docking poses predicted by the balanced and electrostatic scoring algorithms almost all  
377 correspond to symmetry-related locations and poses on F-actin (Extended Data Fig. 3e). In addition, the  
378 predicted orientation of CH2 molecules on F-actin is consistent with the known binding site of the CH1  
379 domain, as judged by the length of the linker that would be required to join the C-terminus of the docked  
380 CH1 domain to the N-terminus of the docked CH2 domain (Extended Data Fig. 3f). Our model predicts that  
381 neither the T59 residue nor its mutated version are directly involved in F-actin binding (Extended Data Fig.  
382 3d). On the CH2 domain, the H275R mutant may result in a stronger interaction with negatively charged  
383 D51 in F-actin (Extended Data Fig. 3e), which may further contribute to its higher actin binding propensity  
384 (Fig. 3d and Extended Data Fig. 2c). We also modeled the missense mutations in the SR (Extended Data  
385 Fig. 3g,h). Except for F344L, all SR variants face outwards, to the solvent, indicating that they could be  
386 involved in protein binding at the interface. Interestingly, all mutations within the second and third helices  
387 of the spectrin fold are neutral or more hydrophobic for the variants, and those in the first helix of the SR  
388 are more hydrophilic. Given the consistency of this trend, we suspect that it may underlie a conserved  
389 functional role important for heterodimerization and larger order assemblies.

390 In sum, our modeling results provide a strong molecular rationale for the biochemical and cellular  
391 observations described above, which implicate protein stability, abnormal assembly and dynamics of the  
392  $\beta$ II-spectrin-F-actin skeleton, and potential disruptions of  $\beta$ II-spectrin binding to other molecular partners,  
393 consistent with similar LOF and GOF changes observed in other members of the spectrin  
394 superfamily<sup>37,40,43</sup>.

395  **$\beta$ II-spectrin mutations disrupt neuron architecture and function**

396 Individual with *SPTBN1* variants display developmental deficits and a wide range of neurological  
397 phenotypes, which implicate  $\beta$ II-spectrin in neuronal development and cerebral cortex function. These  
398 clinical presentations are consistent with phenotypes of neural progenitor-specific  $\beta$ II-spectrin null mice  
399 that lack  $\beta$ II-spectrin throughout brain development<sup>26</sup>. In addition, cortical and hippocampal neurons from  
400 these mice show disruption of the spectrin-actin membrane periodic structure<sup>24</sup>, impaired axonal  
401 formation and growth, and reduced axonal organelle transport, all deficits that can be rescued by  
402 expression of WT  $\beta$ II-spectrin<sup>26,44</sup>. These reports, together with our initial cellular and molecular  
403 observations shown above, suggest that mutant  $\beta$ II-spectrin may result in defects in the organization and  
404 the dynamics of the neuronal submembrane skeleton, and the morphology and function of neurons. Thus,  
405 we next investigated the neuronal effects of human  $\beta$ II-spectrin mutations using a structure-function  
406 rescue approach in  $\beta$ II-SpKO cortical neurons.

407 First, we expressed WT and mutant GFP- $\beta$ II Sp together with mCherry in day in vitro (DIV) 3  $\beta$ II-SpKO  
408 cortical neurons<sup>26</sup> and evaluated their neuronal growth at DIV8. We also evaluated mCherry-expressing  
409 WT (*Sptbn1*<sup>flox/flox</sup> /+) and heterozygous (*Sptbn1*<sup>flox/+</sup>; Nestin-Cre; henceforth abbreviated as  $\beta$ II-SpHet)  
410 neurons grown in parallel. As previously observed<sup>26</sup>, neuronal growth, quantified through axonal length,  
411 was severely impaired in  $\beta$ II-SpKO neurons, but restored upon expression of WT GFP- $\beta$ II Sp (Fig. 5a,b and  
412 Extended Data Fig. 4a).  $\beta$ II-SpHet neurons grew to roughly only half the length of WT neurons, but their  
413 axons were at least twice as long as  $\beta$ II-SpKO neurons (Fig. 5a,b). Most of the  $\beta$ II-spectrin mutants failed  
414 to rescue axonal length except for p.G1398S and p.E1886Q, which restored growth to WT levels, while  
415 p.A1086T and p.E1110D restored length to heterozygous levels (Fig. 5a,b and Extended Data Fig. 4a).  
416 Remarkably, some of the aberrant morphological features observed in HEK293 cells were also present  
417 and often more markedly displayed in neurons expressing mutant GFP- $\beta$ II Sp. As shown above, p.C183\*,  
418 p.Y190\_R216del, p.G205S, and p.G205D GFP- $\beta$ II Sp mutants were almost exclusively distributed in large

419 protein aggregates localized to the neuronal cell bodies and in some processes (Fig. 3b and Extended Data  
420 Fig. 5a). All other mutants within the CH domain invariably produced extensive aberrant membrane  
421 features in the form of lamellipodia and filopodia around the cell body and along the neuronal processes  
422 (Fig. 6a and Extended Data Fig. 5a). Similarly, the p.A850G mutant resulted in cell bodies and neuronal  
423 processes with expanded membranes extensively decorated with filopodia-like protrusions, while the  
424 p.R411W mutant led to a milder phenotype (Extended Data Fig. 5a). Neuronal membrane expansion was  
425 accompanied by a shift in the boundaries of actin and  $\alpha$ II-spectrin distribution (Fig. 6a). These results  
426 confirm that clinically relevant  $\beta$ II-spectrin mutations can cause marked disruptions in cell morphology,  
427 likely driven by disruptions in the submembrane cytoskeleton organization and dynamics, which may be  
428 a pathogenic factor in *SPTBN1* syndrome.

429 Organelle transport is essential for the maintenance of neuronal processes and viability of neurons and  
430 defects in transport can contribute to the pathology of several neurological diseases<sup>45</sup>. We previously  
431 showed that  $\beta$ II-spectrin promotes normal organelle axonal transport independently of its role assembling  
432 the MPS<sup>26</sup>. Expression of WT  $\beta$ II-spectrin in cultured  $\beta$ II-spectrin null cortical neurons rescues the  
433 processivity, motility, and flux of synaptic vesicles and lysosomes<sup>26</sup>. To evaluate the effects of selected  $\beta$ II-  
434 spectrin mutations on axonal transport, we tracked the dynamics of red fluorescent protein (RFP)-tagged  
435 LAMP1 (an endosome/lysosome vesicles marker) in control,  $\beta$ II-SpKO, and  $\beta$ II-SpHet cortical neurons using  
436 time-lapse video microscopy. As previously observed<sup>26</sup>, loss of  $\beta$ II-spectrin impairs the bidirectional  
437 motility of LAMP1-RFP-positive vesicles and causes significant deficits in their run length and retrograde  
438 velocity (Fig. 5c,d and Extended Data Fig. 4b,c). Remarkably,  $\beta$ II-spectrin haploinsufficiency causes similar  
439 deficits (Fig. 5c,d and Extended Data Fig. 4b,c), indicating that 50% reduction of  $\beta$ II-spectrin levels is not  
440 sufficient to maintain normal organelle transport. As expected<sup>26</sup>, deficits in transport of lysosomes in  $\beta$ II-  
441 SpKO neurons are rescued by expression of WT GFP $\beta$ II-Sp. However, selected mutants that do not rescue  
442 axonal length also fail to restore normal organelle dynamics (Fig. 5c,d and Extended Data Fig. 4b,c). Within

443 the mutants tested, p.E892\* and p.W1787\* lack the PH domain, which is required for  $\beta$ II-spectrin coupling  
444 to organelle membranes and normal organelle transport<sup>25</sup>. It is possible that the abnormal binding to  
445 molecular partners observed in other mutants unable to rescue organelle dynamics interfere with the  
446 formation of complexes between  $\beta$ II-spectrin and molecular motors, its coupling to organelle membranes,  
447 or its cytosol to MPS partitioning.

448 Collectively, our results suggest that human  $\beta$ II-spectrin mutations we report likely cause *SPTBN1*  
449 syndrome through molecular and cellular mechanisms that include the individual or combined effects of  
450 toxic protein aggregation, disruption of intracellular organelle transport, insufficient axonal growth, and  
451 aberrant cytoskeletal organization and dynamics, which in turn may affect neuronal connectivity and  
452 function.

#### 453 ***SPTBN1* variant classification**

454 The *SPTBN1* variants described in this study were classified using the 2015 ACMG Guidelines<sup>46</sup> and  
455 interpretation recommendations<sup>47-49</sup> and are listed in Supplementary Table 2 with a summary of  
456 functional evidence herein. Of the 28 unique variants in the cohort, 14 were classified as pathogenic, 12  
457 as likely pathogenic, and two as variants of uncertain significance (VUS). Importantly, proband P10 has  
458 two *de novo* variants in *cis* in *SPTBN1*, p.T268A and p.F344L. The p.T268A variant has two allelic variants  
459 p.T268N and p.T268S and functional studies suggesting a damaging effect support a pathogenic  
460 classification. The p.F344L variant is classified as a VUS since it is in *cis* with a pathogenic variant and  
461 showed no significant differences from wild type in functional studies, thus its contribution to the  
462 phenotype of this individual is unclear.

#### 463 **$\beta$ II-spectrin haploinsufficiency causes cell-autonomous deficits in neuronal connectivity**

464  $\beta$ II-spectrin is widely expressed in both neurons and in brain non-neuronal cells<sup>50</sup>.  $\beta$ II-spectrin loss in both  
465 neurons and glial cells of  $\beta$ II-SpKO mice results in significant reduction of long-range axonal tracts in the

466 cerebellum and of those tracts connecting cerebral hemispheres, including the CC<sup>26</sup>. These white matter  
467 connectivity deficits are likely caused by the impaired axonal growth of neurons lacking  $\beta$ II-spectrin<sup>26</sup>.  
468 Since  $\beta$ II-spectrin haploinsufficiency affects axonal growth *in vitro* (Fig. 5a, b), we next assessed cortical  
469 axonal connectivity in  $\beta$ II-SpHet mice. Consistent with a diminished axonal growth, PND25  $\beta$ II-SpHet mice  
470 exhibit callosal hypoplasia (Fig. 6b,c). CC thinning is also detected by MRI in three of the probands in this  
471 cohort (P2, P10, and P28) (Fig. 1d and Table 1 and Supplementary Note), which further implicates  $\beta$ II-  
472 spectrin in regulating brain cytoarchitecture. Deficits in connectivity of long axonal tracts can also result  
473 from defects in neuronal migration and axonal pathfinding, which in turn can be affected by non-neuronal  
474 cells<sup>51</sup>. To determine the neuron-specific effects of  $\beta$ II-spectrin depletion on cortical wiring, we generated  
475 mice lacking  $\beta$ II-spectrin only in cortical and hippocampus projection neurons by crossing *Sptbn1*<sup>flox/flox</sup> to  
476 Nex-Cre<sup>52</sup> animals (*Sptbn1*<sup>flox/flox</sup>;Nex-Cre; henceforth referred to as  $\beta$ II-Sp-Nex KO) (Extended Data Fig. 5b).  
477  $\beta$ II-spectrin loss or haploinsufficiency only in projection neurons is sufficient to induce CC hypoplasia (Fig.  
478 6c,d). These results suggest that partial  $\beta$ II-spectrin LOF can produce neuronal miswiring in the cortex and  
479 those defects are at least in part neuron-autonomous.

#### 480 **$\beta$ II-spectrin deficiency causes developmental and behavioral deficits in mice**

481 Individuals bearing *SPTBN1* variants exhibit a wide range of facial dysmorphisms, brain growth defects,  
482 including microcephaly and macrocephaly, and DD (Table 1, Supplementary Note). We found that  
483 embryonic day 19 (E19)  $\beta$ II-SpKO mice have enlarged head circumference, and both E19  $\beta$ II-SpKO and  $\beta$ II-  
484 SpHet animals exhibit increased distance between the eyes (Fig. 7a-c), consistent with the observed  
485 hypertelorism in some of the patients (Fig. 1c and Supplementary Note). In line with reported DD in  
486 patients,  $\beta$ II-SpKO mice show arrested development (Fig. 7d,e)<sup>26</sup>. In addition,  $\beta$ II-spectrin  
487 haploinsufficiency is sufficient to yield animals of an intermediate body size and weight (Fig. 7d-f). The  
488 global DD changes observed in mice with  $\beta$ II-spectrin deficits arise in part due to neuronal-autonomous

489 effects, given that they are also observed in  $\beta$ II $\text{Sp-NexKO}$  mice that only lack the protein in cortical and  
490 hippocampal projection neurons (Extended Data Fig. 6a).

491 Since individuals carrying *SPTBN1* variants present with various behavioral phenotypes, including ASD,  
492 ADHD as well as learning and mild motor deficits (Table 1, Supplementary Note), we assessed behavioral  
493 effects of brain  $\beta$ II-spectrin deficiency in mice. First, we evaluated the effects of complete LOF using  $\beta$ II-  
494 SpKO mice. Because these animals do not survive longer than five weeks<sup>26</sup>, they were only challenged  
495 with open field and acoustic startle tests at PND30.  $\beta$ II-SpKO mice had overt hyperactivity at every time  
496 point during the open field test (Fig. 7g) and profound deficits in rearing, a response requiring good hind  
497 limb function and balance (Fig. 7h).  $\beta$ II-SpKO mice also showed decreases in startle response amplitudes  
498 in the acoustic startle test, but normal levels of prepulse inhibition (PPI) (Extended Data Fig. 6b,c),  
499 suggesting that reduced startle responses were due to motor deficits, rather than alterations in auditory  
500 function or sensorimotor gating. This is consistent with impaired motor abilities likely due to the severe  
501 loss of cerebellar connectivity in these mice<sup>26</sup>.

502 Our clinical, cellular, and animal data indicates that  $\beta$ II-spectrin haploinsufficiency, or the altered function  
503 of only one copy of *SPTBN1* due to GOF or dominant-negative effects, is sufficient to cause a  
504 neurodevelopmental disorder. Thus, we next characterized behavioral phenotypes of  $\beta$ II-SpHet mice,  
505 whose normal lifespan allowed for an expanded battery of tests. In contrast to  $\beta$ II-SpKO mice,  $\beta$ II-SpHet  
506 animals had normal activity during an open field test (Fig. 7i,l). Further,  $\beta$ II-SpHet and control mice had  
507 comparable performance in an acoustic startle test for PPI and in the rotarod test (Extended Data Fig. 6d-  
508 f), indicating that expression of half levels of  $\beta$ II-spectrin is sufficient to rescue motor problems.  $\beta$ II-SpHet  
509 mice also exhibited normal spatial and reversal learning in the Morris water maze test (Extended Data Fig.  
510 6g,h). On the other hand, in the 3-chamber choice test,  $\beta$ II-SpHet demonstrated no preference for  
511 spending more time in proximity to a stranger mouse versus an empty cage and made significantly fewer  
512 entries into the side containing the stranger mouse (Fig. 7k,l). These genotype differences were not

513 observed in the subsequent test for social novelty preference, in which  $\beta$ II-SpHet and  $\beta$ II-SpWT littermates  
514 demonstrated the typical shift in preference to the newly introduced stranger 2 (Extended Data Fig. 6k,l).  
515 Notably, there was a non-significant trend for the  $\beta$ II-SpHet mice to make fewer entries than the littermate  
516 controls in the social novelty test. The lack of sociability in the  $\beta$ II-SpHet mice was not associated with  
517 changes in anxiety-like behavior or olfactory function (Extended Data Fig. 7m). Overall, these results  
518 suggest that  $\beta$ II-spectrin LOF impairs global development and has a selective impact on social motivation  
519 and reward that may contribute to the autistic features and social behavior impairments manifested in  
520 some affected individuals.

## 521 Discussion

522 In this study, we report for the first time the identification of *de novo* *SPTBN1* variants in individuals as a  
523 cause of a neurodevelopmental disorder most commonly characterized by motor and speech delays, ID,  
524 and various neurologic and behavioral comorbidities. In addition to DD and ID, eleven individuals in our  
525 cohort have been diagnosed with ADD/ADHD and six with ASD, with three having co-occurrence. This  
526 observation is consistent with a recent WES study of a Danish cohort of approximately 8,000 children with  
527 ASD and/or ADHD and 5,000 controls that identified *SPTBN1* as a top hit among genes with rare truncating  
528 variants co-occurring in these disorders at a significantly higher rate than in controls<sup>53</sup>. *SPTBN1* variants  
529 had previously been reported in probands with ASD<sup>29</sup>, Tourette<sup>28</sup>, and DD (all included in our study).  
530 Noteworthy,  $\beta$ II-spectrin's canonical partner ankyrin-B is encoded by high confidence ASD gene *ANK2*<sup>27</sup>  
531 and some ASD patients with *ANK2* variants also exhibit ID<sup>54</sup>. Loss of ankyrin-B isoforms in mice result in  
532 axonal transport deficits<sup>55</sup> and developmentally regulated defects in brain connectivity<sup>54,55</sup>, two  
533 overlapping phenotypes we observed in our  $\beta$ II-spectrin mouse models. Although ankyrin-B and  $\beta$ II-  
534 spectrin are independent modulators of axonal transport<sup>26</sup>, *SPTBN1* and *ANK2* may otherwise converge  
535 through mechanisms that affect other neuronal functions. For example, loss of ankyrin-B affects the  
536 polarized distribution of  $\beta$ II-spectrin in neurites, which gives rise to its more even portioning between

537 axons and dendrites causing a higher than normal prevalence of the MPS in dendrites<sup>56</sup>. Conversely,  
538 disruption of the MPS due to loss of  $\beta$ II-spectrin<sup>24,26</sup> may disrupt the periodic distribution of ankyrin-B and  
539 its membrane partners in axons<sup>54</sup>, which together may be essential for critical signal transduction events<sup>57</sup>.  
540 In addition to their strong correlation with DD, our results together with these observations support the  
541 association of *SPTNB1* pathogenic variants with ASD and ADHD.

542 Seizures and epilepsy were other noticeable re-occurring phenotypes in our cohort. That *SPTNB1* variants  
543 may have epileptogenic effects is not surprising, given the strong association of *de novo* and inherited  
544 variants in the partner gene *SPTAN1* ( $\alpha$ II-spectrin) with epileptic syndromes<sup>5,16-21</sup>. Although the precise  
545 pathogenic mechanism of *SPTAN1* in epilepsy is unknown,  $\alpha$ II-spectrin protein aggregation has been  
546 reported for several of the putative pathogenic variants<sup>16,20</sup>. As we show above,  $\alpha$ II-spectrin cellular  
547 distribution can be disrupted by mutant  $\beta$ II-spectrin to cause these partners to co-aggregate, or otherwise  
548 continue to associate in aberrant cellular patterns. Since  $\beta$ II- and  $\alpha$ II-spectrin are critically involved in  
549 localizing and stabilizing ion channels<sup>1-3</sup>, going forward it will be critical to elucidate whether these tightly  
550 intertwined partners share pathways disrupted in channelopathies underlying seizures and epilepsy.

551 Besides the widely shared DD phenotype in our cohort, further supporting evidence of the pathogenicity  
552 of *SPTNB1* variants is the re-occurrence of *de novo* variants in the same amino acid position in unrelated  
553 individuals which are not found in the general population. These individuals share other co-occurring  
554 clinical manifestations, but also diverge in some of the clinical presentations, which may originate in part  
555 by differences in the identity of the amino acid substitution, sex, age, and genetic background. Another  
556 striking indicator of convergence in the pathogenic mechanism of the  $\beta$ II-spectrin mutations we report is  
557 their partial clustering (14 of 28) within the CH domains. The region of *SPTNB1* encoding the CH domains  
558 has a higher degree of missense variant constraint in the population (ExAC v.10)<sup>58</sup>, indicating the  
559 importance of the CH domains for protein function and supporting the pathogenicity of the variants  
560 within. Our cellular and biochemical findings suggest that CH domain mutants generally affect  $\beta$ II-

561 spectrin's interaction with F-actin and  $\alpha$ II-spectrin and result in modified spectrin/actin cytoskeleton  
562 dynamics and cellular morphology. The aberrant accumulation of mutant  $\beta$ II-spectrin within cytosolic  
563 aggregates suggests that a subset of the CH mutations introduce destabilizing effects on the protein  
564 structure, which is supported by our structural modeling. These changes in  $\beta$ II-spectrin distribution, as  
565 well as in binding to submembrane cytoskeleton partners, likely underlie GOF effects, such as aberrant  
566 neuronal membrane morphology, and contribute to LOF deficits, such as impaired organelle transport and  
567 reduced axonal growth. In turn, these cellular defects likely result in the deficient or aberrant brain  
568 connectivity and function observed in  $\beta$ II-spectrin-deficient mice and in patients. Interestingly, pathogenic  
569 CH domain variants have been reported in  $\beta$ I-spectrin<sup>59</sup>, which cause spherocytosis, and  $\beta$ III-spectrin<sup>4,13</sup>,  
570 which leads to cerebellar ataxia, DD, and ID, and have been shown to affect F-actin binding<sup>41</sup>. Together  
571 with our results, this evidence indicates that the abnormal modulation of actin binding by CH domain  
572 variants likely constitute a conserved pathogenic mechanism in spectrinopathies.

573 Like in other spectrinopathies<sup>4-23</sup>, missense mutations affecting SR are likely to be disease-causing in the  
574 *SPTBN1* syndrome, although the molecular mechanisms are not fully understood. For example, it is not  
575 clear how p.A850G phenocopies the cellular phenotypes caused by some of the CH domain mutants. It is  
576 possible that this mutant affects  $\beta$ II-spectrin/F-actin dynamics through allosteric mechanisms or dominant  
577 negative effects due to overexpression. Alternatively, this and the other SR mutants may disrupt  $\beta$ II-  
578 spectrin association with undefined binding partners or its coupling to organelles and motor proteins,  
579 which may explain their detrimental effect on axonal growth<sup>26</sup>. Our cellular assays failed to identify a  
580 potential pathogenic mechanism for a small subset of *SPTBN1* variants. However, it is possible that these  
581 variants affect other less explored neuronal  $\beta$ II-spectrin roles, such as dendritic and postsynaptic  
582 development and function, which are associated with ASD<sup>29</sup>. Additionally, given the wide expression of  
583  $\beta$ II-spectrin in non-neuronal brain cells, it will be of interest to assess if their function is affected by *SPTBN1*  
584 variants. It is likely that the clinical variability is at least partly rooted in the multifunctionality and

585 ubiquitous expression of  $\beta$ II-spectrin, although we cannot rule out that some clinical manifestations  
586 unique to affected individuals in the cohort may be caused by an alternate etiology. For example, a few  
587 individuals in the cohort have additional genetic variants that might be contributing to their clinical  
588 phenotype. Proband P19 has a pathogenic *NF1* variant (NM\_000267.3:c.3449C>G; p.S1150\*) and has  
589 neurofibromatosis, which could also have associated learning disabilities, but likely would not explain the  
590 behavioral challenges and autism seen in this individual. Proband P27 has a variant in *GNB1*  
591 (NM\_001282539.1:c.700-1G>T) inherited from her mother also affected with delays. However, the  
592 *SPTBN1* variant was not present in the mother, and could be *de novo* or paternal as her father has  
593 moderate ID, suggesting both variants could be contributory. Finally, given the critical roles  $\beta$ II-spectrin  
594 plays in other organs<sup>60,61</sup> and its association with other non-neurological disorders, including clinical  
595 presentations beyond the nervous system in patients in our cohort, the *SPTBN1* syndrome warrants  
596 thorough clinical assessment and further studies beyond the brain.

## 597 **Materials and methods**

### 598 **Identification of Pathogenic *SPTBN1* Variants**

599 Pathogenic variants in *SPTBN1* were identified by whole exome or genome sequencing performed on  
600 whole blood DNA from probands identified through diagnostic clinical practice or Institutional Review  
601 Board approved research studies. Affected individuals were identified through professional  
602 communication, connections through GeneMatcher<sup>62</sup>, and by searching the Undiagnosed Diseases  
603 Network (UDN) and the Deciphering Developmental Disorders (DDD) Research Study<sup>29</sup> repositories.  
604 Variants were reported according to standardized nomenclature defined by the reference human genome  
605 GRCh37 (hg19) and *SPTBN1* transcript GenBank: NM\_003128.2. The minor-allele frequency of each  
606 variant was determined from genomic sequencing data derived from the gnomAD.

### 607 **Patient consent**

608 Patient consent for participation and phenotyping was obtained through the referring clinical teams.  
609 Referring clinicians were requested to complete a comprehensive questionnaire that was based upon our  
610 current understanding of the phenotypic associations of *SPTBN1*. They included sections related to  
611 neurodevelopmental screening, behavior, dysmorphology, muscular, cardiac, and other systemic  
612 phenotypic features. Consent and collection of information conformed to the recognized standards of the  
613 Declaration of Helsinki and approved by local Institutional Review Boards.

#### 614 **Variant interpretation and classification**

615 *SPTBN1* variants were interpreted using the NM\_003128.2 transcript and splice variants were evaluated  
616 using SpliceAI<sup>27</sup> to predict the most likely mRNA splicing outcome. The *SPTBN1* variants identified in this  
617 study were classified according to the ACMG 2015 Guidelines<sup>46</sup>. Based on the recommendations of PVS1  
618 loss-of-function criterion under the ACMG/AMP specifications<sup>47</sup>, PVS1\_strong was used as a maximum  
619 weight of evidence. This is appropriate for this criterion as we have shown moderate clinical validity<sup>48</sup>,  
620 unrelated probands with a consistent phenotype, and robust functional evidence showing that these  
621 nonsense variants remove downstream portions of the protein known to be essential for protein function,  
622 and that both null and haploinsufficient mouse models recapitulate disease phenotypes. The maximum  
623 weight of functional evidence (PS3) used was moderate under the ACMG/ACMP specifications<sup>49</sup>.

#### 624 **Mouse lines and animal care**

625 Experiments were performed in accordance with the guidelines for animal care of the Institutional Animal  
626 Care and Use Committee of the University of North Carolina at Chapel Hill. To generate neural progenitor-  
627 specific  $\beta$ II-spectrin null (*Sptbn1*<sup>flox/flox</sup>/Nestin-Cre,  $\beta$ IIsp-KO) and haploinsufficient (*Sptbn1*<sup>flox/+</sup>/Nestin-Cre,  
628  $\beta$ IIsp-Het) mice, *Sptbn1*<sup>flox/flox</sup> animals, a gift from Dr. Mathew Rasband<sup>50</sup>, were crossed with the Nestin-  
629 Cre mouse line [B6.Cg-Tg(Nes-cre)1Kln/J, stock number 003771; The Jackson Laboratory]. *Sptbn1*<sup>flox/flox</sup>  
630 animals negative for the Cre transgene were used as littermate controls in all experiments. Mice lacking

631  $\beta$ II-spectrin in cortical projection neurons (*Sptbn1*<sup>flox/flox</sup>/Nex-Cre,  $\beta$ II<sup>Sp</sup>-Nex KO) were generated by  
632 crossing *Sptbn1*<sup>flox/flox</sup> and Nex-Cre, a gift from Dr. Klaus-Armin Nave<sup>52</sup>, animals for multiple generations.  
633 All mice were housed at 22°C  $\pm$  2°C on a 12-hour-light/12-hour-dark cycle and fed ad libitum regular chow  
634 and water.

#### 635 **Generation of human $\beta$ II-spectrin mutations**

636 The human  $\beta$ II-spectrin cDNA was subcloned into peGFP-C3 vector (Clontech) using HindIII and SacI sites  
637 to generate the peGFP- $\beta$ II<sup>Sp</sup> plasmid. For purification of full-length  $\beta$ II-spectrin proteins, both a  
638 prescission protease site (LEVLFGQP) and a 6x histidine tag were respectively introduced between the GFP  
639 and start codon and before the C-terminal stop codon of peGFP- $\beta$ II-spectrin using site-directed  
640 mutagenesis to generate the peGFP-PP- $\beta$ II-<sup>Sp</sup>-6xHis construct. peGFP- $\beta$ II<sup>Sp</sup> and peGFP-PP- $\beta$ II-<sup>Sp</sup>-6xHis  
641 plasmids bearing the human mutations included in the study were generated using the In-Fusion HD  
642 Cloning Plus system (Takara) and primers specific for each mutation site (Supplementary Table 3). All  
643 plasmids were verified by full-length sequencing.

#### 644 **Plasmids**

645 Plasmid used in transfection experiments included: pLAMP1-RFP (Addgene plasmid #1817, gift from  
646 Walther Mothes), pmCherry-C1 (Clontech) and peGFP-C3 vector (Clontech). To generate mCherry-tagged  
647  $\alpha$ II-spectrin (pmCherry- $\alpha$ II<sup>Sp</sup>), the cDNA sequence of human  $\alpha$ II-spectrin (NM\_001130438.3) was  
648 amplified by PCR as a BsrGI/XhoI fragment and cloned into the corresponding sites of pmCherry-C1  
649 (Clontech). peGFP-C3-Y1874A- $\beta$ II-spectrin and HA-tagged 220 kDa ankyrin-B (pAnkB-3X HA) plasmids  
650 were previously reported.<sup>26</sup> All plasmids were verified by full-length sequencing prior to transfection.

#### 651 **Antibodies**

652 Affinity-purified rabbit antibodies against GFP and  $\beta$ II-spectrin, used at a 1:500 dilution for  
653 immunohistochemistry and 1:5000 for western blot, were generated by Dr. Vann Bennett laboratory and

654 have been previously described.<sup>26,51</sup> Other antibodies used for western blot analysis and  
655 immunoprecipitation included mouse anti-GFP (1:1000, #66002-1-Ig), rabbit anti-GFP (1:1000, #50430-2-  
656 AP), rabbit anti-HA tag (1:1000, #51064-2-AP), and mouse anti-6\*His tag (1:1000, # 66005-1-Ig) all from  
657 Proteintech, and rabbit anti-mCherry (1:2000, #ab24345) from Abcam. Commercial antibodies used for  
658 immunofluorescence included mouse anti-neurofilament (1:200, # 837801) from BioLegend and chicken  
659 anti-GFP (1:1000, #GFP-1020) from Aves. Secondary antibodies purchased from Life Technologies were  
660 used at 1:400 dilution for fluorescence-based detection by confocal microscopy, and included donkey  
661 anti-rabbit IgG conjugated to Alexa Fluor 568 (#A10042), donkey anti-mouse IgG conjugated to Alexa Fluor  
662 488 (#A21202), goat anti-chicken conjugated to Alexa Fluor 488 (#A11039), and donkey anti-rat IgG  
663 conjugated to Alexa Fluor 647 (#A21247). Fluorescent signals in western blot analysis were detected using  
664 goat anti-rabbit 800CW (1:15000, #926-32211) and goat anti-mouse 680RD (1:15000, #926-68070) from  
665 LICOR.

#### 666 **Neuronal culture**

667 Primary cortical neuronal cultures were established from E17 mice. Cortices were dissected in Hibernate  
668 E (Life Technologies) and digested with 0.25% trypsin in HBSS (Life Technologies) for 20 min at 37°C. Tissue  
669 was washed three times with HBSS and dissociated in DMEM (Life Technologies) supplemented with 5%  
670 fetal bovine serum (FBS, Genesee), and gently triturated through a glass pipette with a fire-polished tip.  
671 Dissociated cells were filtered through a 70 µm cell strainer to remove any residual non-dissociated tissue  
672 and plated onto poly-D-lysine-coated 1.5 mm coverglasses or dishes (MatTek) for transfection and time-  
673 lapse microscopy imaging. For all cultures, media was replaced 3 hours after plating with serum-free  
674 Neurobasal-A medium containing B27 supplement (Life Technologies), 2 mM Glutamax (Life  
675 Technologies), and penicillin/streptomycin (Life Technologies). 5 µM cytosine-D-arabinofuranoside  
676 (Sigma) was added to the culture medium to inhibit the growth of glial cells three days after plating.  
677 Neurons were fed twice a week with freshly made culture medium until use.

678 **Plasmid transfection for time-lapse live imaging and immunofluorescence analysis**

679 For time-lapse imaging experiments DIV5 cortical neurons were co-transfected with 1 $\mu$ g of each pLAMP1-  
680 RFP and peGFP- $\beta$ II $\text{Sp}$  plasmids using lipofectamine 2000 (Life Technologies) and imaged 48-96 hours after  
681 transfection. For experiments that evaluate axonal length, DIV3 control and  $\beta$ II $\text{Sp}$ -Het neurons were  
682 transfected with 500 ng of pmCherry-C1 and 1 $\mu$ g of peGFP-C3.  $\beta$ II-SpKO neurons were transfected with  
683 500 ng of pmCherry-C1 and 1 $\mu$ g of peGFP- $\beta$ II $\text{Sp}$  rescue plasmids bearing full-length wildtype of mutant  $\beta$ 2-  
684 spectrin. Neurons were processed for immunofluorescence 5 days after transfection.  
685 Immunofluorescence evaluations of  $\beta$ II-spectrin distribution in HEK293 cells was conducted in cells  
686 transfected with 100 ng of peGFP- $\beta$ II $\text{Sp}$  plasmids, or co-transfected with 100  
687 ng of each peGFP- $\beta$ II $\text{Sp}$  and pmCherry- $\alpha$ II $\text{Sp}$  plasmids 48 hours post-transfection.

688 **Plasmid transfection for biochemistry analysis**

689 All transfections were conducted in HEK293 cells grown in 10 cm culture plates using the calcium  
690 phosphate transfection kit (Takara). To purify full-length  $\beta$ II-spectrin proteins, cells were transfected with  
691 8  $\mu$ g of peGFP-PP- $\beta$ II-Sp-6xHis plasmids. To determine levels and stability of  $\beta$ II-spectrin proteins, HEK293T  
692 cells were co-transfected with 8  $\mu$ g of eGFP-PP- $\beta$ II-Sp-6xHis and 4  $\mu$ g of pmCherry-C1 plasmids. To  
693 determine interaction between ankyrin-B and  $\beta$ II-spectrin, cells were co-transfected with 8 $\mu$ g of each  
694 peGFP-PP- $\beta$ II-Sp-6xHis and pAnkB-3X HA plasmids. For assessment of binding between  $\beta$ II-spectrin and  
695  $\alpha$ II-spectrin, cells were separately transfected with 8  $\mu$ g of peGFP-PP- $\beta$ II-Sp-6xHis or 4  $\mu$ g peGFP-C3 and 8  
696  $\mu$ g of pmCherry- $\alpha$ II $\text{Sp}$ .

697 **Histology and immunohistochemistry**

698 Brains from mice two-weeks and older were fixed by transcardial perfusion with phosphate-buffered  
699 saline (PBS) and 4% paraformaldehyde (PFA) followed by overnight immersion in the same fixative. Brains  
700 from PND0-PND14 mice were fixed by direct immersion in 4% PFA for 36 hours. After fixation, brains were

701 rinsed with PBS, transferred to 70% ethanol for at least 24 hours, and paraffin-embedded. 7- $\mu$ m coronal  
702 and sagittal brain sections were cut using a Leica RM2155 microtome and mounted on glass slides.  
703 Sections were analyzed by hematoxylin and eosin (H&E) staining or immunostaining. For antibody  
704 staining, sections were deparaffinized and rehydrated using a standard protocol of washes: 3  $\times$  3-min  
705 Xylene washes, 3  $\times$  2-min 100% ethanol washes, and 1  $\times$  2-min 95%, 80%, and 70% ethanol washes  
706 followed by at least 5 min in PBS. Sections were then processed for antigen retrieval using 10 mM sodium  
707 citrate, pH 6 in the microwave for 20 min. Sections were allowed to cool, washed in PBS, and blocked  
708 using antibody buffer (2% bovine serum albumin (BSA), 1% fish oil gelatin, 5% donkey serum, and 0.02%  
709 Tween 20 in PBS) for 1 hour at room temperature. Tissue sections were then subsequently incubated  
710 overnight with primary antibodies at 4°C and with secondary antisera for 1.5 hours at 4°C, washed with  
711 PBS, and mounted with Prolong Gold Antifade reagent (Life Technologies). Neuronal cultures and HEK293  
712 cells were washed with cold PBS, fixed with 4% PFA for 15 min, and permeabilized with 0.2% Triton-X100  
713 in PBS for 10 min at room temperature. Neurons and HEK293 cells were blocked in antibody buffer for 1  
714 hour at room temperature and processed for fluorescent staining as tissue sections. For actin labeling,  
715 Alexa Fluor 568- or Alexa Fluor 633-conjugated phalloidin (1:100) was added to the secondary antibody  
716 mix. DAPI was added to the last PBS rinse for nuclei staining.

#### 717 **Immunoblots**

718 Protein homogenates from mouse brains or transfected cells were prepared in 1:9 (wt/vol) ratio of  
719 homogenization buffer (8M urea, 5% SDS (wt/vol), 50mM Tris pH 7.4, 5mM EDTA, 5mM N-ethylmeimide,  
720 protease and phosphatase inhibitors) and heated at 65°C for 15 min to produce a clear homogenate. Total  
721 protein lysates were mixed at a 1:1 ratio with 5x PAGE buffer (5% SDS (wt/vol), 25% sucrose (wt/vol),  
722 50mM Tris pH 8, 5mM EDTA, bromophenol blue) and heated for 15 min at 65°C. Samples were resolved  
723 by SDS-PAGE on 3.5-17.5% acrylamide gradient gels in Fairbanks Running Buffer (40mM Tris pH 7.4, 20mM  
724 NaAc, 2mM EDTA, 0.2%SDS (wt/vol)). Proteins were transferred overnight onto 0.45  $\mu$ m nitrocellulose

725 membranes (#1620115, BioRad) at 4°C. Transfer efficiency was determined by Ponceau-S stain.  
726 Membranes were blocked in TBS containing 5% non-fat milk for 1 hour at room temperature and  
727 incubated overnight with primary antibodies diluted in antibody buffer (TBS, 5% BSA, 0.1% Tween-20).  
728 After 3 washes in TBST (TBS, 0.1% Tween-20), membranes were incubated with secondary antibodies  
729 diluted in antibody buffer for two hours at room temperature. Membranes were washed 3x for 10 minutes  
730 with TBST and 2x for 5 minutes in TBS. Protein-antibody complexes were detected using the Odyssey® CLx  
731 Imaging system (LI-COR).

### 732 **Immunoprecipitation**

733 For immunoprecipitation experiments, total protein homogenates from transfected HEK293 cells were  
734 prepared in TBS containing 150 mM NaCl, 0.32 M sucrose, 2 mM EDTA, 1% Triton X-100, 0.5% NP40, 0.1%  
735 SDS, and complete protease inhibitor cocktail (Sigma). Cell lysates were incubated with rotation for 1 hour  
736 at 4°C and centrifuged at 100,000 x g for 30 min. Soluble fractions were collected and precleared by  
737 incubation with Protein-G magnetic beads (#1614023, Bio-Rad) for 1 hour in the cold. Samples were  
738 subjected to immunoprecipitation in the presence of protein-G magnetic beads/antibody or protein-G  
739 magnetic beads/isotype control complexes overnight at 4°C. Immunoprecipitation samples were resolved  
740 by SDS-PAGE and western blot and signal detected using the Odyssey® CLx imaging system.

### 741 **Purification of full-length $\beta$ II-spectrin proteins**

742 Ten 10-cm plates of HEK293 cells expressing each peGFP-PP- $\beta$ II-Sp-6xHis construct were used per  
743 purification. Total protein homogenates from transfected HEK293 cells were prepared in TBS containing  
744 150 mM NaCl, 0.32 M sucrose, 2 mM EDTA, 1% Triton X-100, 0.5% NP40, 0.1% SDS, and complete protease  
745 inhibitor cocktail (Sigma) (IP buffer). Cell lysates were incubated with rotation for 1 hour at 4°C and  
746 centrifuged at 100,000 x g for 30 min. Soluble fractions were incubated overnight with Protein A/G  
747 magnetic beads (#88802, Life Technologies) coupled to GFP antibodies with rotation at 4°C. Beads were

748 extensively washed with IP buffer, followed by washes in TBS containing 300 mM NaCl, and TBS. Full-  
749 length  $\beta$ II-spectrin proteins were eluted from GFP-protein A/G magnetic beads by incubation with HRV-  
750 3C protease, which cleaves between GFP and the start codon of  $\beta$ II-spectrin in prescission protease buffer  
751 (25 mM HEPES, 150 mM NaCl, 1 mM EDTA, 1 mM DTT) for 36 hours at 4°C. The efficiency of cleavage and  
752 purity of the eluates was analyzed by western blot using validated antibodies specific for  $\beta$ II-spectrin and  
753 GFP and 6\*His tags, and by Coomassie blue stain. Eluates were concentrated using Pierce™ Protein  
754 Concentrators PES.

#### 755 **Pulldown assays**

756 For detection of  $\beta$ II-spectrin/ $\alpha$ II-spectrin complexes, control and mutant GFP- $\beta$ II Sp proteins were coupled  
757 to GFP-bound Protein-A/G magnetic beads and incubated with lysates from HEK293 cells expressing  
758 mCherry- $\alpha$ II Sp in IP buffer overnight at 4°C. Beads complexes were washed sequentially with IP buffer,  
759 followed by washes in TBS containing 400 mM NaCl, and TBS. Proteins were eluted in 5x PAGE loading  
760 buffer and analyzed by SDS-PAGE and western blot.

#### 761 **Actin co-sedimentation assay**

762 Interaction between purified full-length  $\beta$ II-spectrin proteins and actin was evaluated using the Actin  
763 Binding Protein Spin-Down Biochem Kit (#BK001, Cytoskeleton) following the manufacturer's  
764 recommendations. In brief, full-length  $\beta$ II-spectrin (1 mg/ml) and  $\alpha$ -actinin (20 mg/ml, positive control)  
765 were prepared in general actin buffer (5 mM Tris-HCl pH 8.0 and 0.2 mM  $\text{CaCl}_2$ ) and centrifuged at 150,000  
766 x g for 1 h at 4°C. F-actin (1 mg/ml) was prepared by incubation of purified actin in general actin buffer for  
767 30 min on ice followed by the actin polymerization step in actin polymerization buffer (50 mM KCl, 2 mM  
768  $\text{MgCl}_2$ , 1 mM ATP) for 1 hour at 24°C. F-actin (21  $\mu\text{M}$ ) was incubated with either  $\beta$ II-spectrin (10  $\mu\text{M}$ ),  $\alpha$ -  
769 actinin (2  $\mu\text{M}$ ), or BSA (2  $\mu\text{M}$ , negative control) for 30 min at 24°C. F-actin-protein complexes were pelleted

770 by ultracentrifugation at 150,000 x g for 1.5 h at 24°C. The presence of F-actin together with interacting  
771 proteins was assessed in the supernatant and pellet fractions by SDS-PAGE and Coomassie blue stain.

## 772 **Fluorescence image acquisition and image analysis**

773 Confocal microscope images were taken using a Zeiss LSM780 using 405-, 488-, 561-, and 633-nm lasers.  
774 Single images and Z-stacks with optical sections of 1 µm intervals and tile scans were collected using the  
775 ×10 (0.4 NA) and ×40 oil (1.3 NA) objective lens. Images were processed, and measurements taken and  
776 analyzed, using Zeiss Zen, Volocity (Perkin Elmer), or NIH ImageJ software. Three-dimensional rendering  
777 of confocal Z-stacks was performed using Imaris (Bitplane).

## 778 **Time-lapse video microscopy and movie analyses**

779 Live microscopy of neuronal cultures was carried out using a Zeiss 780 laser scanning confocal microscope  
780 (Zeiss) equipped with a GaAsP detector and a temperature- and CO<sub>2</sub>-controlled incubation chamber.  
781 Movies were taken in the mid-axon and captured at a rate of 1 frame/second for time intervals ranging  
782 from 60-300 seconds with a 40x oil objective (1.4NA) using the zoom and definite focus functions. Movies  
783 were processed and analyzed using ImageJ (<http://rsb.info.nih.gov/ij>). Kymographs were obtained  
784 using the KymoToolBox plugin for ImageJ  
785 ([https://github.com/fabricecordelieres/IJ\\_KymoToolBox](https://github.com/fabricecordelieres/IJ_KymoToolBox)). In details, space (x axis in µm) and time (y axis  
786 in sec) calibrated kymographs were generated from video files. In addition, the KymoToolBox plugin was  
787 used to manually follow a subset of particles from each kymograph and report the tracked particles on  
788 the original kymograph and video files using a color code for movement directionality (red for  
789 anterograde, green for retrograde and blue for stationary particles). Quantitative analyses were  
790 performed manually by following the trajectories of individual particles to calculate dynamic parameters  
791 including, net and directional velocities and net and directional run length, as well as time of pause or  
792 movement in a direction of transport. Anterograde and retrograde motile vesicles were defined as

793 particles showing a net displacement  $>3 \mu\text{m}$  in one direction. Stationary vesicles were defined as particles  
794 with a net displacement  $<2 \mu\text{m}$ .

### 795 **Statistical analysis**

796 GraphPad Prism (GraphPad Software) was used for statistical analysis. Two groups of measurements were  
797 compared by unpaired Student's t test. Multiple groups were compared by one-way ANOVA followed by  
798 a Dunnett's multiple comparisons test.

### 799 **Molecular modeling of *SPTBN1* Variants**

800 We used the closed conformation of utrophin CH1-CH2 closed dimer (PDB 1qag)<sup>39</sup> as a template for the  
801 analogous  $\beta$ II-spectrin conformation to estimate its electrostatic surface profile. Molecular structures  
802 from the 6.9 Å cryo-EM structure of the CH1 actin-binding domain of  $\beta$ III-spectrin bound to F-actin (PDB  
803 ID 6anu)<sup>41</sup> and the structure of the CH2 domain of  $\beta$ II-spectrin (PDB ID 1bkr)<sup>40</sup> were used for protein-  
804 protein docking predictions. The ClusPro protein-protein docking webserver<sup>42,43</sup> was used to 1) dock the  
805 CH1 domain of spectrin onto F-actin, 2) dock the CH2 domain of spectrin onto F-actin, and 3) dock the  
806 CH2 domain of spectrin onto the CH1 domain of spectrin. The CH1 structure used for the dockings  
807 reported here was the model of the CH1 domain of  $\beta$ III-spectrin from 6anu (chain a)<sup>41</sup>. This CH1 model  
808 was built based on the crystal structure of plectin (PDB ID 1mb8)<sup>63</sup> by I-TASSER<sup>64</sup>. The CH1 domain of  $\beta$ III-  
809 spectrin shares 95% sequence identity with the CH1 domain of  $\beta$ II-spectrin. The actin model corresponded  
810 to chains A-F of 6anu, which in turn was generated from the cryo-EM structure of actin (PDB ID 5jlh)<sup>65</sup>.  
811 The molecular structure of the CH2 domain of  $\beta$ II-spectrin from 1bkr was of a 1.1 Å crystal structure<sup>40</sup>.

812 To identify the inactive closed conformation of the tandem domain (CH1-CH2) of  $\beta$ II-spectrin, the CH2  
813 domain of  $\beta$ II-spectrin was docked onto the CH1 domain of  $\beta$ II-spectrin using the ClusPro webserver. The  
814 top 15 docking poses for each of the four scoring algorithms were evaluated for the placement of  $\beta$ II-  
815 spectrin residue L250 from the CH2 domain at the interface of the CH2/CH1 closed conformation. The top

816 docking pose in the electrostatic scoring algorithm corresponded to a pose with a deeply buried L250 at  
817 the interface of the CH1/CH2 complex. The mutation of the equivalent residue in  $\beta$ III-spectrin (L253P)  
818 might disrupt the closed structure and drive the spectrin ensemble to a more open state suitable for  
819 binding to actin<sup>40</sup>. This same docking pose was also a top docking pose (pose 4) within the set of poses  
820 calculated by the balanced scoring algorithm. This pose was used for evaluation of the  $\beta$ II-spectrin  
821 mutants. It was also the same pose compared to the actinin-4 (PDB ID 6oa6) (unpublished) and utrophin  
822 (PDB ID 1qag)<sup>39</sup> closed conformations.

823 For each of the three ClusPro protein docking analyses, the webserver provided up to 30 docking poses  
824 for each of four scoring algorithms (balanced; electrostatic-favored; hydrophobic-favored; VdW+Elec).  
825 The top 15 poses from each of the four scoring algorithms were included in the final analysis. For the  
826 dockings of the CH1 and CH2 domains from  $\beta$ II-spectrin onto F-actin, several of the top docking poses  
827 were to the ends of the actin segment defined as the receptor. These docking poses were immediately  
828 rejected as other actin molecules would be binding at those locations in F-actin and these sites would not  
829 be available for binding to spectrin. For CH1 docking onto F-actin, the remaining poses within the top eight  
830 docking poses predicted by the balanced and electrostatic scoring algorithms almost all corresponded to  
831 the location and orientation of CH1 molecules on actin as defined by the cryo-EM structure 6anu. For CH2  
832 docking onto F-actin, the remaining poses within the top 8 docking poses predicted by the balanced and  
833 electrostatic scoring algorithms almost all corresponded to symmetry-related locations and poses on the  
834 F-actin. In addition, the predicted orientation of the CH2 molecules on F-actin was consistent with the  
835 known binding site of the CH1 domains, as judged by the length of the linker that would be required to  
836 join the C-terminus of the docked CH1 domain to the N-terminus of the docked CH2 domain.

837  $\beta$ II-spectrin is a large multi-domain protein that requires a different approach for each type of domain.  
838 The SR have relatively low sequence identity to each other, and only a few have been experimentally  
839 solved, requiring independent models to be generated for each. We used RaptorX<sup>66</sup> homology modeling

840 to generate each model and assembled them into a linear conformation using Discovery Studio [Dassault  
841 Systèmes BIOVIA, Discovery Studio Modeling Environment, Release 2019, San Diego: Dassault Systèmes.  
842 2019]. We calculated protein electrostatics using APBS<sup>67</sup> and visualized structures using PyMOL [The  
843 PyMOL Molecular Graphics System, Version 2.0.7 Schrödinger, LLC.]. Individual spectrin repeats were also  
844 superimposed onto each other using a geometric algorithm<sup>68</sup> as implemented in PyMOL, to investigate  
845 patterns across the fold.

#### 846 **Behavioral assessment**

847 **Animals.** Because the *Sptbn1*<sup>flox/flox</sup>/Nestin-Cre ( $\beta$ II-SpKO) mice have early mortality (typically between  
848 PND30 and PND40), testing in these mice was conducted late in the juvenile period. Subjects were 15  
849 wildtype (*Sptbn1*<sup>flox/flox</sup>/+,  $\beta$ II-SpWT) and 5  $\beta$ II-SpKO mice, taken from 5 litters.  $\beta$ II-SpKO mice were  
850 evaluated in two tests: open field (at PD 28-31) and acoustic startle (at PD 29-32). *Sptbn1*<sup>flox/+</sup>/Nestin-Cre  
851 ( $\beta$ II-SpHet), which have normal survival rates, were subjected to a more expansive battery of tests.  $\beta$ II-  
852 SpHet mice (n=12 per genotype, all males) underwent the following tests, with order planned so that more  
853 stressful procedures occurred closer to the end of the study.

854 <b>Age (wk)</b>	<b>Procedure</b>
855 <b>5</b>	Elevated plus maze test for anxiety-like behavior
856 <b>6</b>	Locomotor activity and exploration in a 1-hr open field test
857 <b>7</b>	Rotarod test for motor coordination and motor learning
858 <b>8-9</b>	Social approach in a three-chamber choice test
859 <b>9-10</b>	Marble-bury assay for anxiety-like behavior and perseverative responses
860	Prepulse inhibition of acoustic startle responses
861 <b>10-11</b>	Buried food test for olfactory ability

862      **11-12**                      Morris water maze; visible platform test for vision and swimming ability

863      **12-13**                      Water maze, hidden platform test for spatial learning

864      **13-14**                      Reversal learning in water maze

865      **Elevated plus maze.** A five-min test for anxiety-like behavior was carried out on the plus maze (elevation,  
866      50 cm H; open arms, 30 cm L; closed arms, 30 cm L, walls, 20 cm H). Mice were placed in the center (8 cm  
867      x 8 cm) at the beginning of the test. Measures were taken of percent open arm time and open arm entries,  
868      and total number of arm entries.

869      **Open field.** Exploratory activity was evaluated by a 1-hr test (30-min for  $\beta$ II-SpKO mice) in a novel open  
870      field chamber (41 cm x 41 cm x 30 cm) crossed by a grid of photobeams (VersaMax system, AccuScan  
871      Instruments). Counts were taken of photobeam breaks in 5-min intervals, with separate measures for  
872      locomotor activity (total distance traveled) and vertical rearing movements. Anxiety-like behavior was  
873      assessed by measures of time spent in the center region.

874      **Accelerating rotarod.** Mice were first given three trials on the rotarod (Ugo Basile, Stoelting Co.), with 45  
875      seconds between each trial. Two additional trials were conducted 48 hr later, to evaluate consolidation  
876      of motor learning. Rpm (revolutions per minute) progressively increased from 3 to a maximum of 30 rpm.  
877      across five minutes (the maximum trial length), and latency to fall from the top of the rotating barrel was  
878      recorded.

879      **Social approach in a three-chamber choice test.** Mice were evaluated for the effects of *Sptbn1* deficiency  
880      on social preference. The procedure had three 10-minute phases: habituation, sociability, and social  
881      novelty preference. In the sociability phase, mice were presented with a choice between proximity to an  
882      unfamiliar C57BL/6J adult male (“stranger 1”), versus an empty cage. In the social novelty phase, mice  
883      were presented with the already-investigated stranger 1 and a new unfamiliar mouse (“stranger 2”). The  
884      test was carried out in a rectangular, three-chambered Plexiglas box (60 cm L, 41.5 cm W, 20 cm H). An

885 automated image tracking system (Noldus Ethovision) provided measures of time spent within 5 cm  
886 proximity to each cage and entries into each side of the social test box.

887 **Marble-burying.** Mice were tested for exploratory digging in a Plexiglas cage, placed inside a sound-  
888 attenuating chamber with ceiling light and fan. The cage floor had 5 cm of corncob bedding, with 20 black  
889 glass marbles (14 mm diameter) set up in a 5 X 4 grid on top of the bedding. Measures were taken of the  
890 number of marbles buried by the end of the 30-min test.

891 **Buried food test.** Mice were presented with an unfamiliar food (Froot Loops, Kellogg Co.) in the home  
892 cage several days before the test. All home cage food was removed 16-24 hr before the test. The assay  
893 was conducted in a tub cage (46 cm L, 23.5 cm W, 20 cm H), containing paper chip bedding (3 cm deep).  
894 One Froot Loop was buried in the cage bedding, and mice were given 15 min to locate the buried food.  
895 Latency to find the food was recorded.

896 **Acoustic startle.** This procedure was used to assess auditory function, reactivity to environmental stimuli,  
897 and sensorimotor gating. The test was based on the reflexive whole-body flinch, or startle response, that  
898 follows exposure to a sudden noise. Mice were evaluated for startle magnitude and prepulse inhibition,  
899 which occurs when a weak prestimulus leads to a reduced startle in response to a subsequent louder  
900 noise. Startle amplitudes were measured by force displacement of a piezoelectric transducer (SR-Lab, San  
901 Diego Instruments). The test had 42 trials (7 of each type): no-stimulus trials, trials with the acoustic  
902 startle stimulus (40 msec; 120 dB) alone, and trials in which a prepulse stimulus (20 msec; either 74, 78,  
903 82, 86, or 90 dB) occurred 100 msec before the onset of the startle stimulus. Levels of prepulse inhibition  
904 at each prepulse sound level were calculated as  $100 - [(response\ amplitude\ for\ prepulse\ stimulus\ and\ startle\ stimulus\ together / response\ amplitude\ for\ startle\ stimulus\ alone) \times 100]$ .  
905

906 **Morris water maze.** The water maze (diameter = 122 cm) was used to assess spatial and reversal learning,  
907 swimming ability, and vision. The procedure had three phases: visible platform, acquisition in the hidden

908 platform task, and reversal learning (with the platform moved to a new location). For each phase, mice  
909 were given 4 60-sec trials per day. Measures were taken of time to find the escape platform (diameter =  
910 12 cm) and swimming velocity by an automated tracking system (Noldus Ethovision). Criterion for learning  
911 was an average group latency of 15 sec or less to locate the platform. At the end of the acquisition and  
912 reversal phases, mice were given a one-min probe trial in the maze without the platform. Selective  
913 quadrant search was evaluated by measuring number of crosses over the location where the platform  
914 (the target) had been placed during training, versus the corresponding areas in the other three quadrants.

### 915 **Statistical Analyses for behavioral tests**

916 All testing was conducted by experimenters blinded to mouse genotype. Statview (SAS, Cary, NC) was  
917 used for data analyses. One-way or repeated measures analysis of variance (ANOVA) were used to  
918 determine effects of genotype. Post-hoc analyses were conducted using Fisher's Protected Least  
919 Significant Difference (PLSD) tests only when a significant F value was found in the ANOVA. For all  
920 comparisons, significance was set at  $p < 0.05$ .

### 921 **Web Resources**

922 Genome Aggregation Database (GnomAD), <https://gnomad.broadinstitute.org/>

923 ClinVar, <https://www.ncbi.nlm.nih.gov/clinvar/>

924 Combined Annotation Dependent Depletion (CADD), <https://cadd.gs.washington.edu/>

925 Mutation Taster, <http://www.mutationtaster.org/>

926 PolyPhen2, <http://genetics.bwh.harvard.edu/pph2/>

927 Protein Variation Effect Analyzer (PROVEAN), <http://provean.jcvi.org/index.php>

928 Sorting Intolerant from Tolerant (SIFT), <https://sift.bii.a-star.edu.sg/>

929 PredictSNP2, <http://loschmidt.chemi.muni.cz/predictsnp2/>

930 M-CAP, <http://bejerano.stanford.edu/mcap/>

### 931 **Acknowledgments**

932 We thank all the families who participated in this study. We thank Drs. Matthew Rasband and Klaus-Armin  
933 Nave for the gift of the  $\beta$ II-spectrin conditional null and the Nex-cre mice, respectively. We thank Dr.  
934 Natallia V. Riddick for her assistance with the behavioral studies. We thank Drs. Beverly Koller and Karen  
935 Mohlke for their insightful comments on this manuscript and Dr. James Bear for helpful discussions.  
936 M.A.C, L.E.S-R., and E.W.K. were supported by the Center for Individualized Medicine at Mayo Clinic.  
937 D.N.L. was supported by the University of North Carolina at Chapel Hill (UNC-CH) School of Medicine as a  
938 Simmons Scholar, by the National Ataxia Foundation, and by the US National Institutes of Health (NIH)  
939 grant R01NS110810. Microscopy was performed at the UNC-CH Neuroscience Microscopy Core Facility,  
940 supported, in part, by funding from the NIH-NINDS Neuroscience Center Grant P30 NS045892 and the  
941 NIH-NICHD Intellectual and Developmental Disabilities Research Center Support Grant U54 HD079124,  
942 which also supported, in part, the behavioral studies. Research reported in this manuscript was supported  
943 by the NIH Common Fund, through the Office of Strategic Coordination/Office of the NIH Director under  
944 Award Number U01HG007672 (Duke University to Dr. Vandana Shashi). The content is solely the  
945 responsibility of the authors and does not necessarily represent the official views of the NIH. This research  
946 was made possible through access to the data and findings generated by the 100,000 Genomes Project.  
947 The 100,000 Genomes Project is managed by Genomics England Limited (a wholly owned company of the  
948 Department of Health and Social Care). The 100,000 Genomes Project is funded by the National Institute  
949 for Health Research and NHS England. The Wellcome Trust, Cancer Research UK and the Medical Research  
950 Council have also funded research infrastructure. The 100,000 Genomes Project uses data provided by  
951 patients and collected by the National Health Service as part of their care and support.

### 952 **Author Contributions**

953 M.A.C. and D.N.L. conceived and planned the study with input from Q.K.T and R.C.S. M.A.C. managed the  
954 collection, analysis, and interpretation of patient clinical data with Q.K.T., R.C.S., and D.N.L. D.N.L.  
955 designed the cell biology, histology, and biochemistry studies, performed these with K. A. B., B. A. C., D.  
956 A., and S. D., and analyzed the data. S.T., M.T.Z., B.T. and D.N.L. performed the structural modeling. K.M.H.  
957 and S.M. performed the mouse behavioral studies. M.C.S. contributed reagents. M.A.C. and D.N.L. wrote  
958 the manuscript with contributions from R.C.S., S.M, M.T.Z, and B.T. E.W.K. and D.N.L. supervised the  
959 study. All other authors including Q.K.T. and R.C.S. contributed clinical data. All authors approved the final  
960 manuscript.

#### 961 **Competing interests**

962 E.T., R. E.P., Y.S., E.A.N., and A.B. are employees of GeneDx, Inc. E.E.E. The authors declare no other  
963 competing interests.

#### 964 **References**

- 965 1. Bennett, V. & Lorenzo, D. N. Spectrin- and ankyrin-based membrane domains and the evolution of  
966 vertebrates. *Curr. Top. Membr.* **72**, 1-37 (2013).
- 967 2. Bennett, V. & Lorenzo, D. N. An adaptable spectrin/ankyrin-based mechanism for long-range  
968 organization of plasma membranes in vertebrate tissues. *Curr. Top. Membr.* **77**, 143-184 (2016).
- 969 3. Lorenzo, D. N. Cargo hold and delivery: Ankyrins, spectrins, and their functional patterning of  
970 neurons. *Cytoskeleton (Hoboken)*, **77**, 129-148 (2020).
- 971 4. Ikeda, Y., et al. Spectrin mutations cause spinocerebellar ataxia type 5. *Nat. Genet.* **38**, 184–190  
972 (2006).

- 973 5. Saitsu, H., et al. Dominant-negative mutations in alpha-II spectrin cause West syndrome with severe  
974 cerebral hypomyelination, spastic quadriplegia, and developmental delay. *Am. J. Hum. Genet.* **86**,  
975 881–891 (2010).
- 976 6. Wang, C. C., et al.  $\beta$ IV spectrinopathies cause profound intellectual disability, congenital hypotonia,  
977 and motor axonal neuropathy. *Am. J. Hum. Genet.* **102**, 1158–1168 (2018).
- 978 7. Jacob, F. D., Ho, E. S., Martinez-Ojeda, M., Darras, B. T. & Khwaja, O. S. Case of infantile onset  
979 spinocerebellar ataxia type 5. *J. Child Neurol.* **28**, 1292–1295 (2013).
- 980 8. Parolin Schnekenberg, R., et al. De novo point mutations in patients diagnosed with ataxic cerebral  
981 palsy. *Brain*, **138**, 1817–1832 (2015).
- 982 9. Nuovo, S., et al. Between SCA5 and SCAR14: delineation of the SPTBN2 p.R480W-associated  
983 phenotype. *Eur. J. Hum. Genet.* **26**, 928–929 (2018).
- 984 10. Nicita, F., et al. Heterozygous missense variants of SPTBN2 are a frequent cause of congenital  
985 cerebellar ataxia. *Clin. Genet.* **96**, 169-175 (2019).
- 986 11. Mizuno, T., et al. Infantile-onset spinocerebellar ataxia type 5 associated with a novel SPTBN2  
987 mutation: A case report. *Brain Development*, **41**, 630-633 (2019).
- 988 12. Accogli, A., et al. Heterozygous missense pathogenic variants within the second spectrin repeat of  
989 SPTBN2 lead to infantile-onset cerebellar ataxia. *J. Child Neurol.* **35**, 106-110 (2019).
- 990 13. Lise, S., et al. Recessive mutations in SPTBN2 implicate  $\beta$ -III spectrin in both cognitive and motor  
991 development. *PLoS Genet.* **8**, e1003074 (2012).
- 992 14. Yıldız Bölükbaşı, E., et al. Progressive SCAR14 with unclear speech, developmental delay, tremor, and  
993 behavioral problems caused by a homozygous deletion of the SPTBN2 pleckstrin homology domain.  
994 *Am. J. Med. Genet. Part A*, **173**, 2494-2499 (2017).

- 995 15. Al-Muhaizea, M., et al. A novel homozygous mutation in SPTBN2 leads to spinocerebellar ataxia in a  
996 consanguineous family: Report of a new infantile-onset case and brief review of the literature.  
997 *Cerebellum*, **17**, 276-285 (2018).
- 998 16. Writzl, K., et al. Early onset West syndrome with severe hypomyelination and coloboma-like optic  
999 discs in a girl with SPTAN1 mutation. *Epilepsia*, **53**, e106–e110 (2012).
- 1000 17. Hamdan, F. F., et al. Identification of a novel in-frame de novo mutation in SPTAN1 in intellectual  
1001 disability and pontocerebellar atrophy. *Eur. J. Hum. Genet.* **20**, 796–800 (2012).
- 1002 18. Nonoda, Y. et al. Progressive diffuse brain atrophy in West syndrome with marked hypomyelination  
1003 due to SPTAN1 gene mutation. *Brain Development*, **35**, 280–283 (2013).
- 1004 19. Tohyama, J., et al. SPTAN1 encephalopathy: distinct phenotypes and genotypes. *J. Hum. Genet.* **60**,  
1005 167-173 (2015).
- 1006 20. Syrbe, S., et al. Delineating SPTAN1 associated phenotypes: from isolated epilepsy to  
1007 encephalopathy with progressive brain atrophy. *Brain*, **140**, 2322-2336 (2017).
- 1008 21. Beijer, D., et al. Nonsense mutations in alpha-II spectrin in three families with juvenile onset  
1009 hereditary motor neuropathy. *Brain*, **142**, 2605-2616 (2019).
- 1010 22. Knierim, E., et al. A recessive mutation in beta-IV-spectrin (SPTBN4) associates with congenital  
1011 myopathy, neuropathy, and central deafness. *Hum. Genet.* **136**, 903-910 (2017).
- 1012 23. Häusler, M. G., et al. A novel homozygous splice-site mutation in the SPTBN4 gene causes axonal  
1013 neuropathy without intellectual disability. *Eur. J. Med. Genet.* **63**, 103826 (2020).
- 1014 24. Xu, K., Zhong, G., Zhuang, X. Actin, spectrin, and associated proteins form a periodic cytoskeletal  
1015 structure in axons. *Science*, **339**, 452-456 (2013).

- 1016 25. Cheney, R., Hirokawa, N., Levine, J., & Willard, M. Intracellular movement of fodrin. *Cell Motility*, **3**,  
1017 649–655 (1983).
- 1018 26. Lorenzo, D.N., et al.  $\beta$ II-spectrin promotes mouse brain connectivity through stabilizing axonal  
1019 plasma membranes and enabling axonal organelle transport. *Proc. Natl. Acad. Sci. U S A.* **116**, 15686-  
1020 15695 (2019).
- 1021 27. Jaganathan, K., et al. Predicting Splicing from Primary Sequence with Deep Learning. *Cell*, **176**, 535-  
1022 548 (2019).
- 1023 28. Willsey, A. J., Fernandez, T. V., Yu, D., et al. De novo coding variants are strongly associated with  
1024 Tourette Disorder. *Neuron*, **94**, 486–499 (2017).
- 1025 29. Firth, H.V., et al. DECIPHER: Database of chromosomal imbalance and phenotype in humans using  
1026 ensembl resources. *Am. J. Hum. Genet.* **84**, 524-533 (2009).
- 1027 30. Iossifov, I., et al. The contribution of de novo coding mutations to autism spectrum disorder. *Nature*,  
1028 **515**, 216–221. (2014).
- 1029 31. Karczewski, K. J., et al. The mutational constraint spectrum quantified from variation in 141,456  
1030 humans. *Nature*, **581**, 434-443 (2020).
- 1031 32. Speicher, D. W., Weglarz, L., DeSilva, T. M. Properties of human red cell spectrin heterodimer (side-  
1032 to-side) assembly and identification of an essential nucleation site. *J. Biol. Chem.* **267**, 14775-14782  
1033 (1992).
- 1034 33. Li, X., Bennett, V. Identification of the spectrin subunit and domains required for formation of  
1035 spectrin/adducin/actin complexes. *J. Biol. Chem.* **271**, 15695-15702 (1996).
- 1036 34. Davis, L., Abdi, K., Machius, M., et al. Localization and structure of the ankyrin-binding site on beta2-  
1037 spectrin. *J. Biol. Chem.* **284**, 6982-6987 (2009).

- 1038 35. Bignone, P. A., Baines, A. J. Spectrin alpha II and beta II isoforms interact with high affinity at the  
1039 tetramerization site. *Biochem. J.* **374**, 613-624 (2003).
- 1040 36. Hyvönen, M., et al. Structure of the binding site for inositol phosphates in a PH domain. *EMBO J.* **14**,  
1041 4676-4685 (1995).
- 1042 37. Korenbaum E, Rivero F. Calponin homology domains at a glance. *J. Cell Sci.* **115**, 3543-3545 (2002).
- 1043 38. Yin, L. M., Schnoor, M., Jun, C. D. Structural characteristics, binding partners and related diseases of  
1044 the calponin homology (CH) domain. *Front. Cell. Dev. Biol.* **8**, 342 (2020).
- 1045 39. Keep NH, Winder SJ, Moores CA, Walke S, Norwood FL, Kendrick-Jones J. Crystal structure of the  
1046 actin-binding region of utrophin reveals a head-to-tail dimer. *Structure*, **7**, 1539-1546 (1999).
- 1047 40. Bañuelos S, Saraste M, Djinović Carugo K. Structural comparisons of calponin homology domains:  
1048 implications for actin binding. *Structure*, **6**, 1419-1431 (1998).
- 1049 41. Avery, A.W., et al. Structural basis for high-affinity actin binding revealed by a  $\beta$ -III-spectrin SCA5  
1050 missense mutation. *Nat. Commun.* **8**, 1350 (2017).
- 1051 42. Vajda, S., et al. New additions to the ClusPro server motivated by CAPRI. *Proteins: Structure,*  
1052 *Function, and Bioinformatics.* **85**, 435-444 (2017).
- 1053 43. Kozakov, D., et al. The ClusPro web server for protein-protein docking. *Nat. Prot.* **12**, 255-278 (2017).
- 1054 44. Galiano, M. R., et al. A distal axonal cytoskeleton forms an intra-axonal boundary that controls axon  
1055 initial segment assembly. *Cell*, **149**, 1125-1139 (2012).
- 1056 45. Sleigh, J. N., Rossor, A. M., Fellows, A. D., Tosolini, A. P., Schiavo, G. Axonal transport and  
1057 neurological disease. *Nat. Rev. Neurol.* **15**, 691-703 (2019).

- 1058 46. Richards, S., et al. Standards and guidelines for the interpretation of sequence variants: a joint  
1059 consensus recommendation of the American College of Medical Genetics and Genomics and the  
1060 Association for Molecular Pathology. *Genet. Med.* **17**, 405-424 (2015).
- 1061 47. Abou Tayoun, A. N., et al. Recommendations for interpreting the loss of function PVS1 ACMG/AMP  
1062 variant criterion. *Hum. Mutat.* **39**, 1517-1524 (2018).
- 1063 48. Strande, N. T., et al. Evaluating the Clinical Validity of Gene-Disease Associations: An Evidence-Based  
1064 framework developed by the Clinical Genome Resource. *Am. J. Hum. Genet.* **100**, 895-906 (2017).
- 1065 49. Brnich, S. E., et al. Recommendations for application of the functional evidence PS3/BS3 criterion  
1066 using the ACMG/AMP sequence variant interpretation framework. *Genome Med.* **12**, 3 (2019).
- 1067 50. Susuki, K., et al. Glial  $\beta$ II spectrin contributes to paranode formation and maintenance. *J. Neurosci.*  
1068 **38**, 6063-6075 (2018).
- 1069 51. Gobius, I. et al. Astroglial-mediated remodeling of the interhemispheric midline is required for the  
1070 formation of the corpus callosum. *Cell Rep.* **17**, 735-747 (2016).
- 1071 52. Goebbels, S., et al. Genetic targeting of principal neurons in neocortex and hippocampus of NEX-Cre  
1072 mice. *Genesis*, **44**, 611-621 (2006).
- 1073 53. Satterstrom, F. K., et al. Autism spectrum disorder and attention deficit hyperactivity disorder have a  
1074 similar burden of rare protein-truncating variants. *Nat. Neurosci.* **22**, 1961-1965 (2019).
- 1075 54. Yang, R. et al. ANK2 autism mutation targeting giant ankyrin-B promotes axon branching and ectopic  
1076 connectivity. *Proc. Natl. Acad. Sci. U S A.* **116**, 15262-15271 (2019).
- 1077 55. Lorenzo, D. N., et al. A PIK3C3–ankyrin-B–dynactin pathway promotes axonal growth and  
1078 multiorganelle transport. *J. Cell Biol.* **207**, 735-752 (2014).

- 1079 56. Zhong, G., et al. Developmental mechanism of the periodic membrane skeleton in axons. *Elife*, **3**,  
1080 e04581 (2014).
- 1081 57. Zhou, R., Han, B., Xia, C., Zhuang, X. Membrane-associated periodic skeleton is a signaling platform  
1082 for RTK transactivation in neurons. *Science*, **365**, 929-934 (2019).
- 1083 58. Lek, M., et al. Analysis of protein-coding genetic variation in 60,706 humans. *Nature*, **536**, 285-291  
1084 (2016).
- 1085 59. Park, J. et al. Mutational characteristics of ANK1 and SPTB genes in hereditary spherocytosis. *Clin.*  
1086 *Genet.* **90**, 69-78 (2016) [published correction appears in *Clin. Genet.* **95**, 341 2019].
- 1087 60. Baek, H. J. et al. Transforming growth factor- $\beta$  adaptor,  $\beta$ 2-spectrin, modulates cyclin dependent  
1088 kinase 4 to reduce development of hepatocellular cancer. *Hepatology*. **53**, 1676-1684 (2011).
- 1089 61. Derbala, M. H., Guo, A. S., Mohler, P. J., Smith, S. A. The role of  $\beta$ II spectrin in cardiac health and  
1090 disease. *Life Sci.* **192**, 278-285 (2018).
- 1091 62. Sobreira, N., Schiettecatte, F., Valle, D., Hamosh, A. GeneMatcher: a matching tool for connecting  
1092 investigators with an interest in the same gene. *Hum. Mutat.* **36**, 928-930 (2015).
- 1093 63. García-Alvarez, B., Bobkov A, Sonnenberg A, de Pereda JM. Structural and functional analysis of the  
1094 actin binding domain of plectin suggests alternative mechanisms for binding to F-actin and integrin  
1095 beta4. *Structure*, **11**, 615-625 (2003).
- 1096 64. Zhang, Y. I-TASSER server for protein 3D structure prediction. *BMC Bioinformatics*, **9**, 40 (2008).
- 1097 65. von der Ecken, J., Heissler, S. M., Pathan-Chhatbar, S., Manstein, D. J., Raunser, S. Cryo-EM structure  
1098 of a human cytoplasmic actomyosin complex at near-atomic resolution. *Nature*, **534**, 724-728  
1099 (2016).

1100 66. Källberg, M., Margaryan, G., Wang, S., Ma, J., Xu, J. RaptorX server: a resource for template-based  
1101 protein structure modeling. *Methods Mol. Biol.* **1137**, 17-27 (2014).

1102 67. Jurrus, E., et al. Improvements to the APBS biomolecular solvation software suite. *Protein Science: a*  
1103 *Publication of the Protein Society.* **27**, 112-128 (2018).

1104 68. Shindyalov, I.N., Bourne, P.E. Protein structure alignment by incremental combinatorial extension  
1105 (CE) of the optimal path. *Protein Eng.* **11**, 739-747 (1998).

## 1106 **Figure Legends**

1107 **Fig. 1: *SPTBN1* variants found in individuals with neurodevelopmental disorders.** **a**, Schematic  
1108 representation of functional domains of  $\beta$ II-spectrin. CH1=calponin homology domain 1 (teal),  
1109 CH2=calponin homology domain 2 (red), SR=spectrin repeat (green), and PH=pleckstrin homology domain  
1110 (purple). The locations of *SPTBN1* variants are indicated. **b**, Alignment of protein sequences for  $\beta$ II-spectrin  
1111 and orthologues show that missense variants identified in the patients in this study are located at highly  
1112 conserved residues across species from humans to *Drosophila*. The position of *SPTBN1* variants analyzed  
1113 in the sequenced of human  $\beta$ II-spectrin is shown for reference. **c**, Photos of individuals with *SPTBN1*  
1114 variants. Ages at the time of photograph are: P8: 7y8m, P9:16, P12: 11y, P13: 6y, P21 left: unknown, Right:  
1115 11y, P22: 15y, P27: 16y11m, P28: 3y11m. **d**, Examples of brain MRI findings: diffuse cerebral parenchymal  
1116 volume loss (L>R) and asymmetric appearance of hippocampi (P1, acquired at <1y), white matter disease  
1117 in the supratentorial and infratentorial regions (P18, acquired at 7y), thinning of the posterior body of the  
1118 corpus callosum without significant volume loss (P28, acquired at 10m).

1119 **Fig. 2: *SPTBN1* variants alter protein expression and subcellular distribution.** **a**, Levels of GFP- $\beta$ II<sub>Sp</sub>  
1120 mutant proteins in HEK293T cells co-transfected with GFP- $\beta$ II<sub>Sp</sub> and mCherry plasmids relative to  
1121 expression of WT GFP- $\beta$ II<sub>Sp</sub>. **b**, Partition of indicated GFP- $\beta$ II<sub>Sp</sub> proteins expressed in HEK293T cells  
1122 between Triton-X100 soluble and insoluble fractions relative to total WT GFP- $\beta$ II<sub>Sp</sub> levels. Data in **b** and **c**

1123 is representative of three independent experiments. All data represent mean  $\pm$  SEM. One-way ANOVA  
1124 with Dunnett's post hoc analysis test for multiple comparisons, \* $p < 0.05$ , \*\*  $p < 0.01$ , \*\*\* $p < 0.001$ , \*\*\*\* $p$   
1125  $< 0.0001$ . **c**, Immunofluorescence images of HEK293T cells transfected with indicated GFP- $\beta$ II $\text{Sp}$  plasmids  
1126 and stained for actin (phalloidin) and DAPI. Scale bar, 10  $\mu\text{m}$ . Expression of variants within the distal end  
1127 of CH1 and the proximal portion of the CH2 domains result in cytosolic GFP-positive aggregates (white  
1128 arrowheads). Expression of variants within the C-terminal portion of the CH2 domain and a subset of  
1129 variants in SRs increase the number of membrane protrusions (white asterisks). Data is representative of  
1130 at least six independent experiments.

1131 **Fig. 3: *SPTBN1* variants alter interaction with critical cytoskeleton partners.** **a**, Immunofluorescence  
1132 images of HEK293T cells transfected with mCherry- $\alpha$ II $\text{Sp}$  and with either WT or mutant GFP- $\beta$ II $\text{Sp}$   
1133 plasmids. Cells were stained for actin (phalloidin) and DAPI. Scale bar, 10  $\mu\text{m}$ . **b**, Immunofluorescence  
1134 images of DIV8 mouse  $\beta$ II $\text{Sp}$ -KO cortical neurons transfected with indicated GFP- $\beta$ II $\text{Sp}$  plasmids and  
1135 stained for actin (phalloidin) and endogenous  $\alpha$ II-spectrin. Scale bar, 5  $\mu\text{m}$ . In **a** and **b** GFP-positive  
1136 cytoplasmic aggregates (orange arrowheads) also contain either actin or  $\alpha$ II-spectrin proteins, or both. **c**,  
1137 Quantification of binding of mCherry- $\alpha$ II $\text{Sp}$  to GFP- $\beta$ II $\text{Sp}$  proteins relative to the abundance of mCherry-  
1138  $\alpha$ II $\text{Sp}$ /WT GFP- $\beta$ II $\text{Sp}$  complexes. **d**, Binding of purified  $\beta$ II-spectrin proteins to purified F-actin assessed  
1139 through an actin co-sedimentation assay. **e**, Binding of GFP- $\beta$ II $\text{Sp}$  proteins to 220-kDa AnkB-2HA assessed  
1140 via co-IP from HEK293T cells. The Y1874A  $\beta$ II-spectrin mutation known to disrupt the formation of AnkB/  
1141  $\beta$ II $\text{Sp}$  complexes was used as control. Graphs in **c** and **d** summarize results from three independent  
1142 experiments. Data in **e** summarizes four independent experiments. All data represent mean  $\pm$  SEM. One-  
1143 way ANOVA with Dunnett's post hoc analysis test for multiple comparisons, \* $p < 0.05$ , \*\*  $p < 0.01$ , \*\*\* $p$   
1144  $< 0.001$ , \*\*\*\* $p < 0.0001$ .

1145 **Fig. 4:  $\beta$ II-spectrin CH domain variants likely alter CH1-CH2 dimer stability.** **a**, Closed conformation of the  
1146  $\beta$ II-spectrin CH1-CH2 dimer modeled after utrophin<sup>37</sup> showing the sites of  $\beta$ II-spectrin variants at the

1147 interface and the electrostatic surface of each domain calculated independently. **b, c**, Electrostatic  
1148 complementarity shows that both CH domains have a polar side, where CH2 is negatively charged (**b**) and  
1149 CH1 is positively charged(**c**), and both have a neutral side. **d**, Closed conformation of the  $\beta$ II-spectrin CH1-  
1150 CH2 dimer modeled by docking the CH2 domain of  $\beta$ II-spectrin<sup>38</sup> onto the CH1 domain modeled after  $\beta$ III-  
1151 spectrin<sup>39</sup>. **e**, The L250R variant introduces a large, positively charged residue that clashes with a  
1152 hydrophobic CH1 pocket through steric hindrance and electric instability. **f**, L247H introduces a large  
1153 aromatic amino acid and likely disrupts normal CH2 folding. **g, h** Steric hindrance and negative charge  
1154 introduced by (**g**) G205D and (**h**) G205S in the interior of CH2 likely disrupts normal CH2 folding. **i**, Key  
1155 interactions at the CH1-CH2 interface (site of mutations in CH1 (teal) and CH2 (red)) and likely molecular  
1156 perturbations caused by *STPBN1* variants.

1157 **Fig. 5: *SPTBN1* variants affect neuronal axonal growth and organelle transport.** **a**, Images of DIV8  $\beta$ II-  
1158 SpWT,  $\beta$ II-SpHet, and  $\beta$ II-SpKO neurons transfected at DIV3 with mCherry. A subset of  $\beta$ II-SpKO neurons  
1159 was co-transfected with GFP- $\beta$ II Sp and mCherry plasmids. Scale bar, 15  $\mu$ m. **b**, Axonal length of  $\beta$ II-SpWT,  
1160  $\beta$ II-SpHet,  $\beta$ II-SpKO, and rescued  $\beta$ II-SpKO DIV8 neurons (n=12-34 neurons/genotype) compiled from  
1161 three independent experiments. Data represent mean  $\pm$  SEM. One-way ANOVA with Dunnett's post hoc  
1162 analysis test for multiple comparisons, \*\*\*\*p < 0.0001. **c**, Kymographs showing the mobility of RFP-tagged  
1163 LAMP1-positive cargo in axons from DIV8  $\beta$ II-SpKO and rescued  $\beta$ II-SpKO neurons. Analyzed trajectories  
1164 are shown with a color code with green for anterograde, red for retrograde, and blue for static vesicles.  
1165 Scale bar, 10  $\mu$ m and 60 s. **d**, Quantification of percent of motile LAMP1-RFP-positive cargo in axons from  
1166  $\beta$ II-SpWT,  $\beta$ II-SpHet,  $\beta$ II-SpKO, and rescued  $\beta$ II-SpKO neurons. The box and whisker plots represent data  
1167 from minimum to maximum collected in n=9-13 axons per genotype. One-way ANOVA with Dunnett's  
1168 post hoc analysis test for multiple comparisons, \*\*\*\*p < 0.0001.

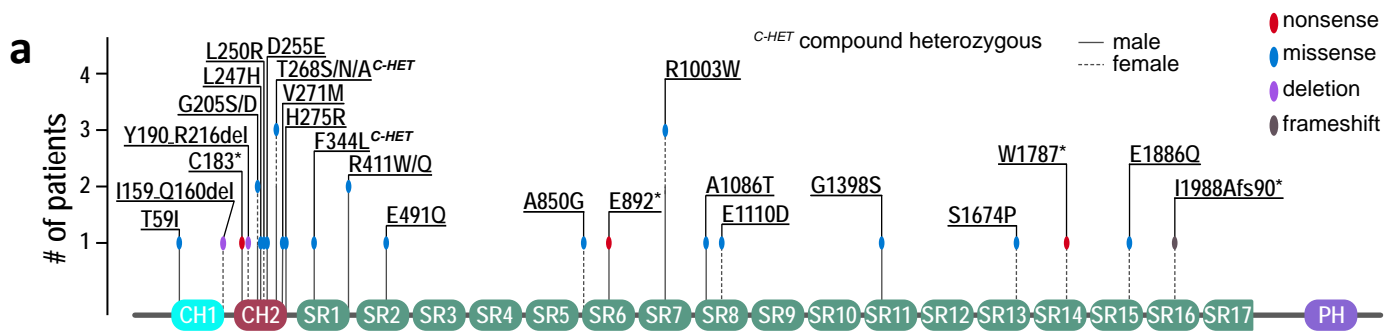
1169 **Fig. 6:  $\beta$ II-spectrin deficiency disrupt proper neuronal development in cortical neuronal cultures and**  
1170 **mouse brains.** **a**, Images of DIV8  $\beta$ II-SpKO cortical neurons rescued with WT GFP- $\beta$ II Sp or with GFP- $\beta$ II Sp

1171 bearing mutations within the distal portion of the CH2 domain. Neurons were stained for actin (phalloidin)  
1172 and endogenous  $\alpha$ II-spectrin. Yellow dotted lines demark the cell edge. Scale bar, 5  $\mu$ m. **b**, Images of  
1173 PND25  $\beta$ II-SpWT and  $\beta$ II-SpHet brains stained for neurofilament to label axons and DAPI. Scale bar, 50  $\mu$ m.  
1174 **c**, Quantification of CC thickness at the brain midline. (n=4 mice/genotype). Data represent mean  $\pm$  SEM.  
1175 Unpaired *t*-test, \**p* < 0.05. **d**, Images of PND25  $\beta$ II-SpNexWT,  $\beta$ II-SpNexHet and  $\beta$ II-SpNexKO brains stained  
1176 for neurofilament to label axons and DAPI. Scale bar, 50  $\mu$ m. White dotted lines in **b** and **d** denote the  
1177 position and boundaries of the corpus callosum (CC). **e**, Quantification of CC thickness at the brain midline.  
1178 (n=6-7 mice/genotype). Data in **c** and **e** represent mean  $\pm$  SEM. One-way ANOVA with Dunnett's post hoc  
1179 analysis test for multiple comparisons, \*\*\**p* < 0.001, \*\*\*\**p* < 0.0001.

1180 **Fig. 7:  $\beta$ II-spectrin deficiency causes developmental and behavioral deficits in mice.** **a**, Images of male  
1181 E19  $\beta$ II-SpWT,  $\beta$ II-SpHet, and  $\beta$ II-SpKO embryos. **b**, **c**, Quantification of head circumference (**b**) and eye  
1182 distance (**c**) at E19. Data represents mean  $\pm$  SEM (n=5-6 embryos/genotype). One-way ANOVA with  
1183 Dunnett's post hoc analysis test for multiple comparisons, \**p* < 0.05, \*\* *p* < 0.01. **d**, Images of male PND25  
1184 wildtype ( $\beta$ II-SpWT) mice and mice with partial ( $\beta$ II-SpHet) and complete ( $\beta$ II-SpKO) loss of  $\beta$ II-spectrin in  
1185 neural progenitors. **e**, Body length at PND25 for indicated genotypes. Data represent mean  $\pm$  SEM (n=12  
1186 male mice/genotype). One-way ANOVA with Dunnett's post hoc analysis test for multiple comparisons,  
1187 \*\*\*\**p* < 0.0001. **f**, Growth curve (as body weight) of  $\beta$ II-SpWT and  $\beta$ II-SpHet mice. Data represent  
1188 mean  $\pm$  SEM (n=12 male mice/genotype). Unpaired *t*-test, \*\* *p* < 0.01, \*\*\**p* < 0.001. **g**, Locomotor activity  
1189 and **h**, rearing assessed during a 30-minutes open-field test in PND30  $\beta$ II-SpWT and  $\beta$ II-SpKO mice. Data  
1190 in **g** and **h** represent mean  $\pm$  SEM (n=15  $\beta$ II-SpWT and n=5  $\beta$ II-SpKO male mice). Unpaired *t*-test, \* *p* < 0.05,  
1191 \*\*\*\**p* < 0.0001. Statistical comparisons were not conducted for **h** due to zero scores in the  $\beta$ II-SpKO  
1192 group. **i**, **j**, Locomotor activity measured as distance traveled (**i**) and number of rears (**j**) during a one-hour  
1193 test in a novel open field. **k**, Lack of social preference in  $\beta$ II-SpHet mice during a three-chamber choice

1194 task. I, Decreased entries by  $\beta$ II-SpHet mice into a chamber with stranger mouse. Data represent  
1195 mean  $\pm$  SEM (n=12 male mice/genotype). Unpaired *t*-test, \**p*< 0.05.

1196 **Table 1. Summary of clinical features observed among *SPTBN1* mutations carriers.** Abbreviations are as  
1197 follows: Ma=male, Female=F, P=partial, C=complete, ID=intellectual disability, \*Emotional Liability  
1198 includes tantrums and depression, Mi=mild, Mo=moderate, S=severe, M-M=mild to moderate, M-  
1199 S=moderate to severe, L-N=low to normal, U=unknown, ND=not diagnosed, NA=not assessed, F=febrile  
1200 seizures only, +=presence, -=absence, ↓= micro or hypo, ↑= macro or hyper, \*\*=half-siblings.

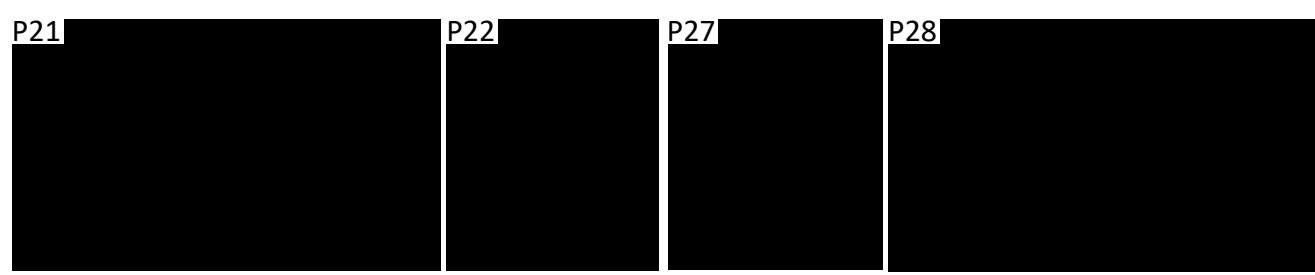
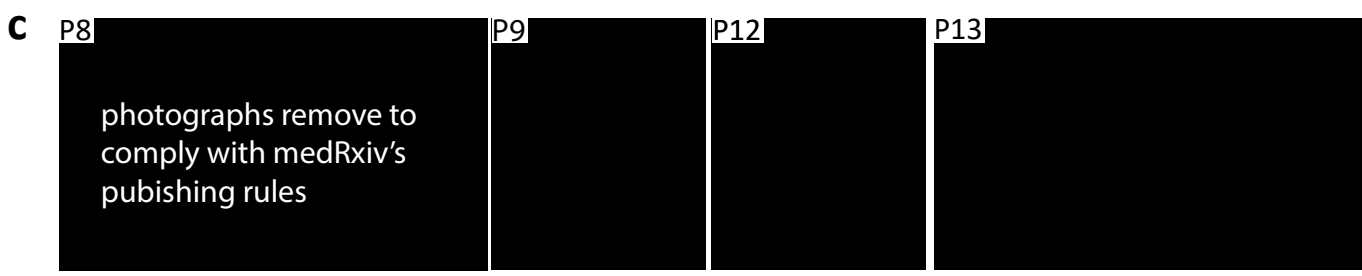


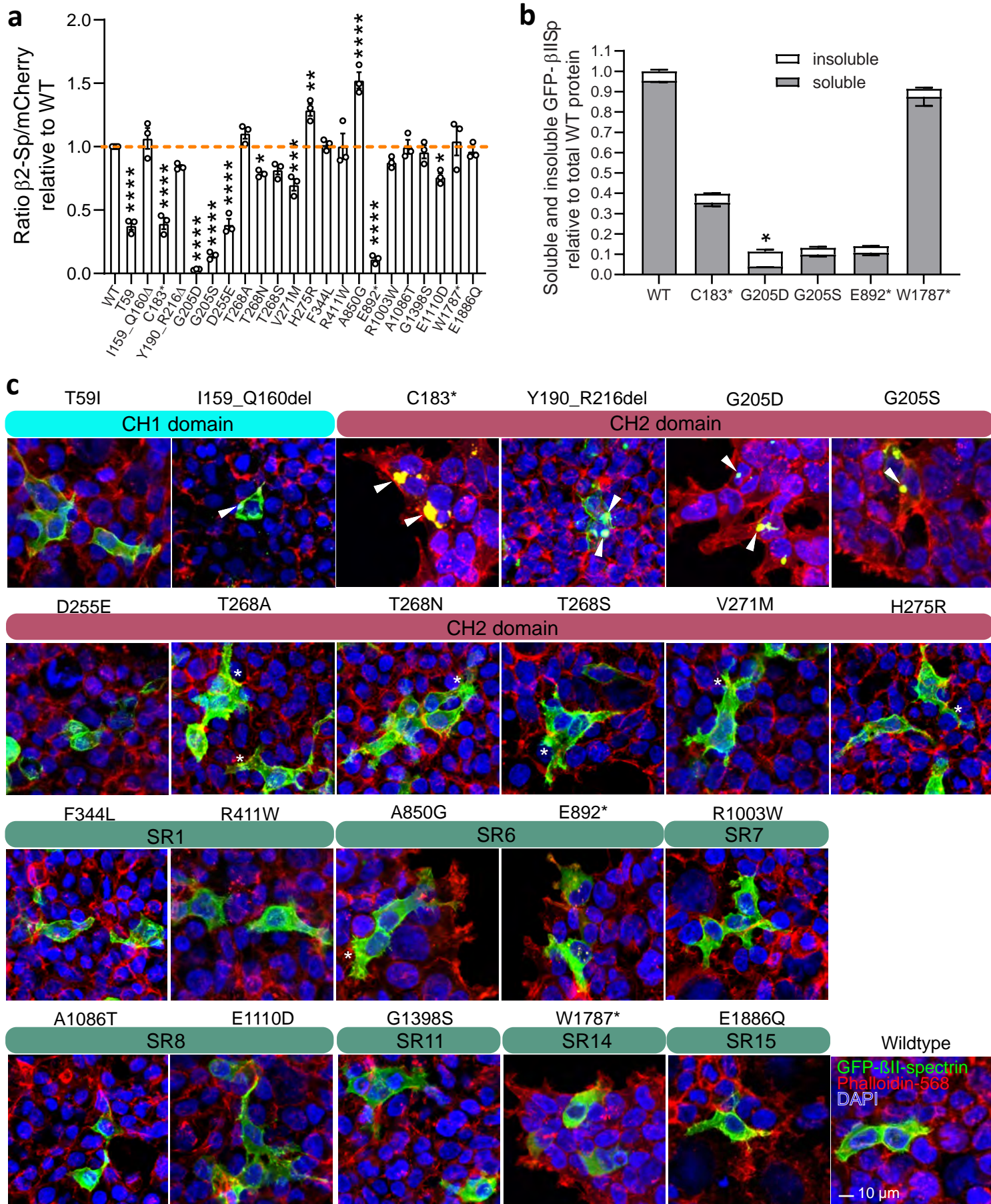
**b**

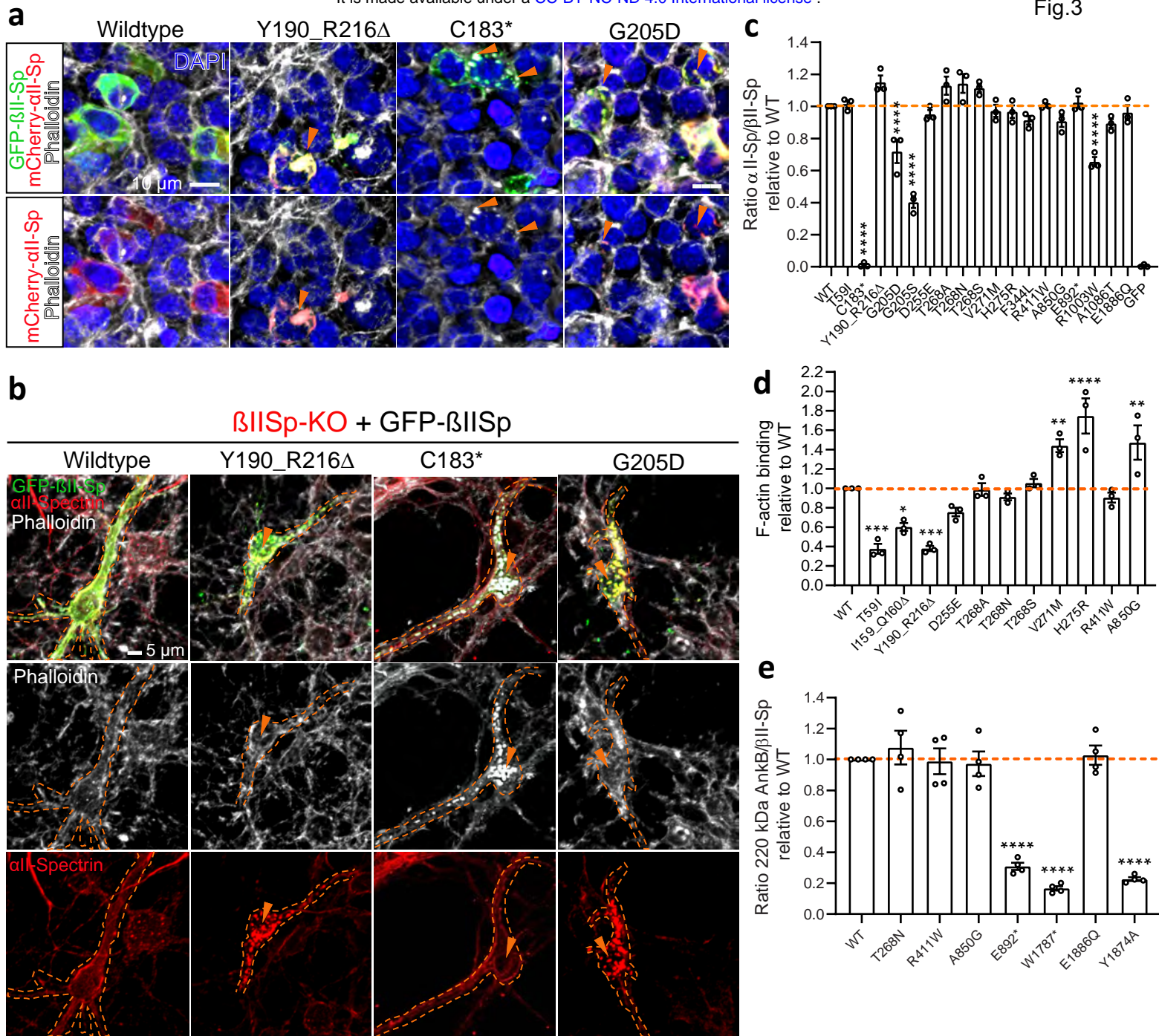
	59	159	183	205	247	250	255	268	271	275	344
Human <i>SPTBN1</i>	KKTFT	FQIQD	LWCQM	RDGMA	LGLTK	TKLLD	PEDIS	IITYV	YVVTY	YYHYF	QAFNT
Chimp <i>SPTBN1</i>	KKTFT	FQIQD	LWCQM	RDGMA	LGLTK	TKLLD	PEDIS	IITYV	YVVTY	YYHYF	QAFNT
Dog <i>SPTBN1</i>	KKTFT	FQIQD	LWCQM	RDGMA	LGLTK	TKLLD	PEDIS	IITYV	YVVTY	YYHYF	QAFNT
Mouse <i>Sptbn1</i>	KKTFT	FQIQD	LWCQM	RDGMA	LGLTK	TKLLD	PEDIS	IITYV	YVVTY	YYHYF	QAFNT
Worm <i>unc-70</i>	KKTFT	FQIQD	LWCQM	RDGLA	LGLAK	AKFLD	PEDIS	IITYV	YVVTY	YYHYF	TEFND
Fly <i>Beta-spec</i>	KKTFT	FQIQD	LWCQM	RDGLA	LGLAK	AKLLD	PEDIS	IITYV	YVVTY	YYHYF	AQFSN

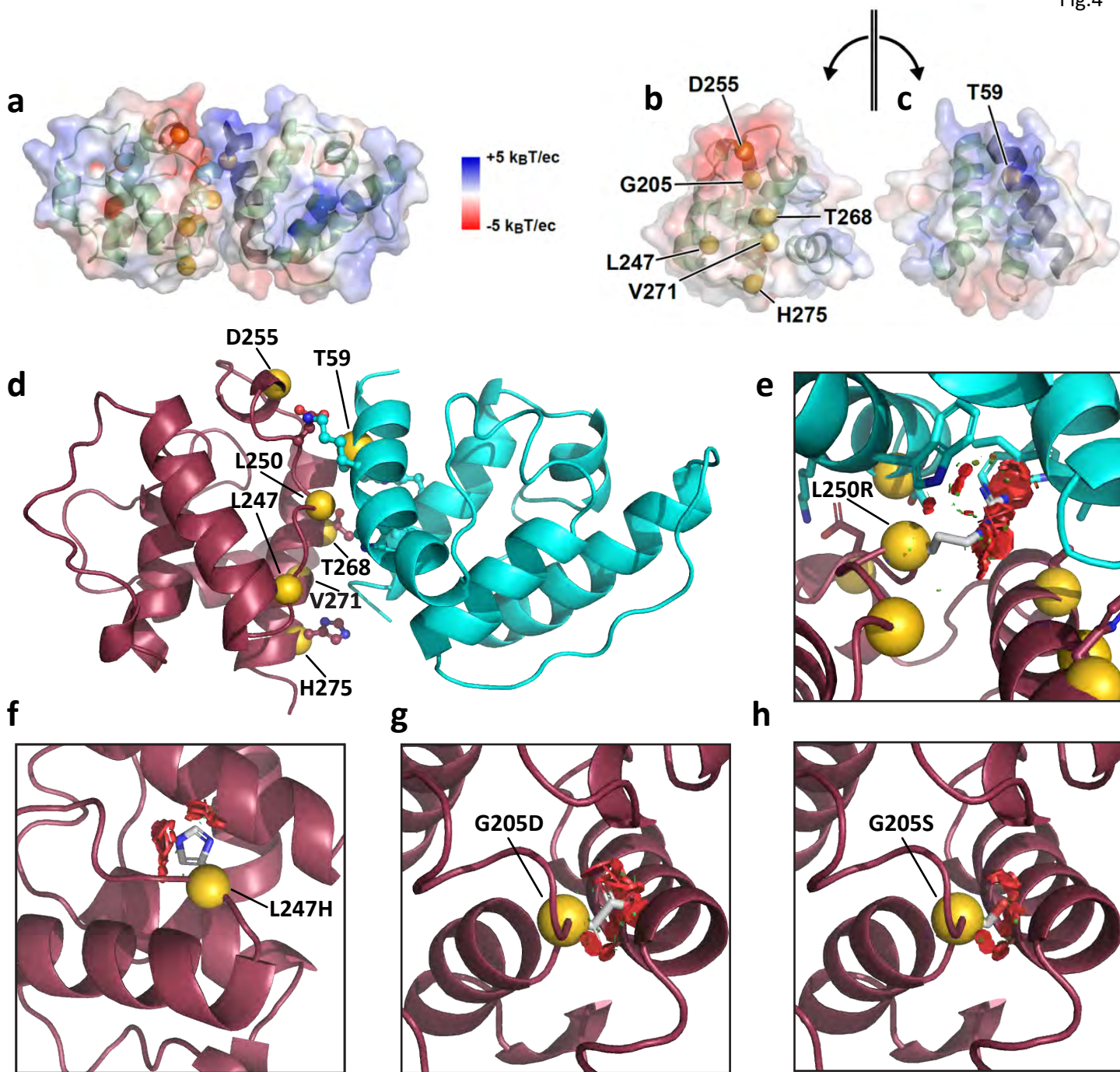
  

	411	491	850	892	1003	1086	1110	1398	1674	1787	1886
Human <i>SPTBN1</i>	ALRNE	EAENY	TLALY	RFESL	MERDL	AIASE	KNEID	LHGLE	RQSKV	EAWAD	KRENE
Chimp <i>SPTBN1</i>	ALRNE	EAENY	TLALY	RFESL	MERDL	AIASE	KNEID	LHGLE	RQSKV	EAWAD	KRENE
Dog <i>SPTBN1</i>	ALRNE	EAENY	TLALY	RFESL	MERDL	AIASE	KNEID	LHGLE	RQSKV	EAWAD	KRENE
Mouse <i>Sptbn1</i>	ALRNE	EAENY	TLALY	RFESL	MERDL	AIASE	KNEID	LHGLE	RQSKV	EAWAD	KRENE
Worm <i>unc-70</i>	VLKEE	EAENY	ALSLY	RFDTL	MERDL	QVASE	REEID	ATQLE	RQAQI	EAWEN	SRESE
Fly <i>Beta-spec</i>	ALREE	ESERY	ALSLY	RFEGF	MDRDL	DVASE	REEID	ITDLE	KQSQL	ESWQD	NREQE



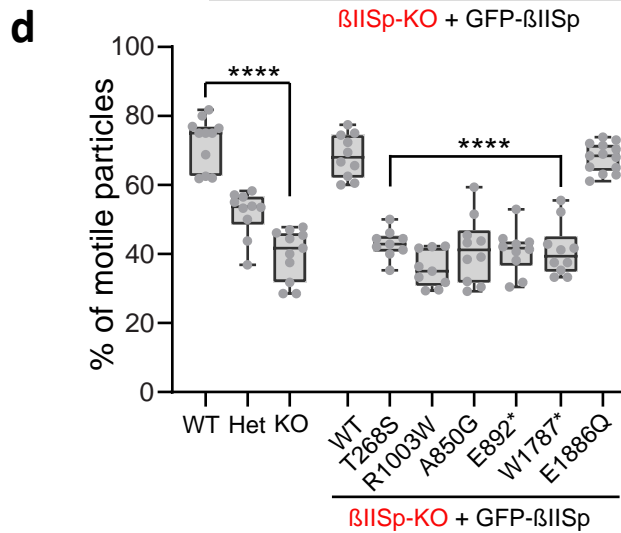
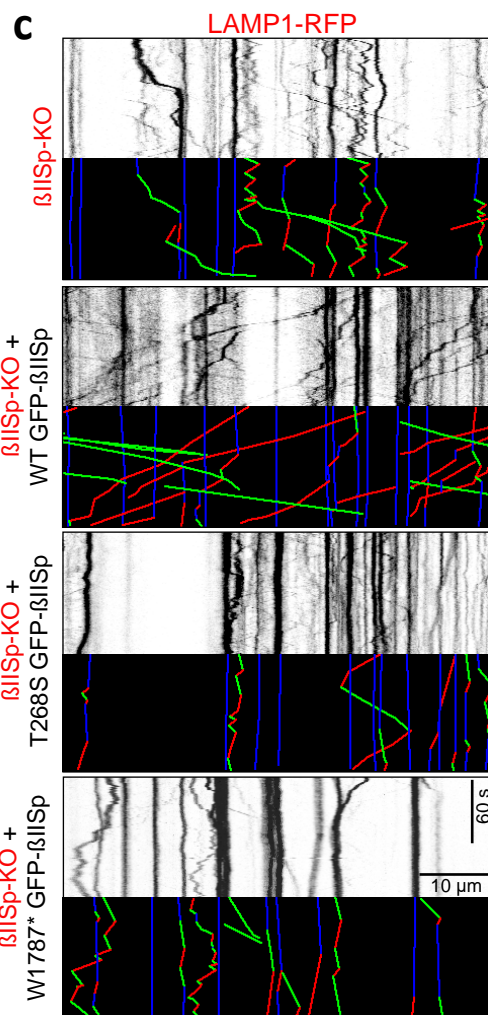
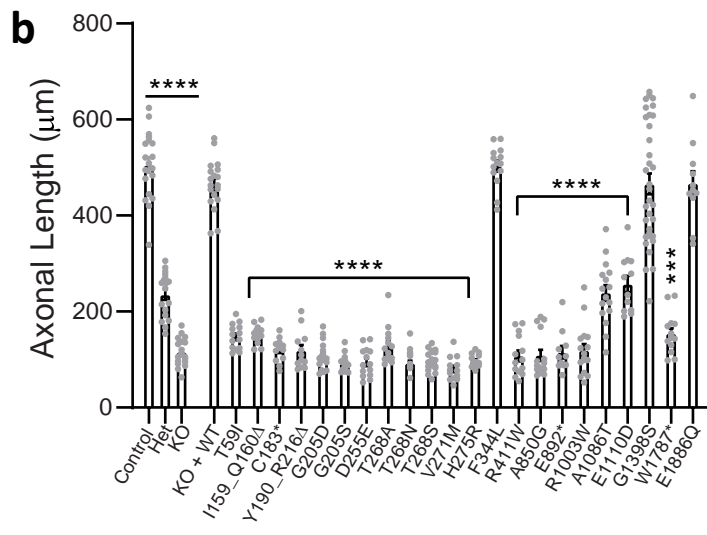
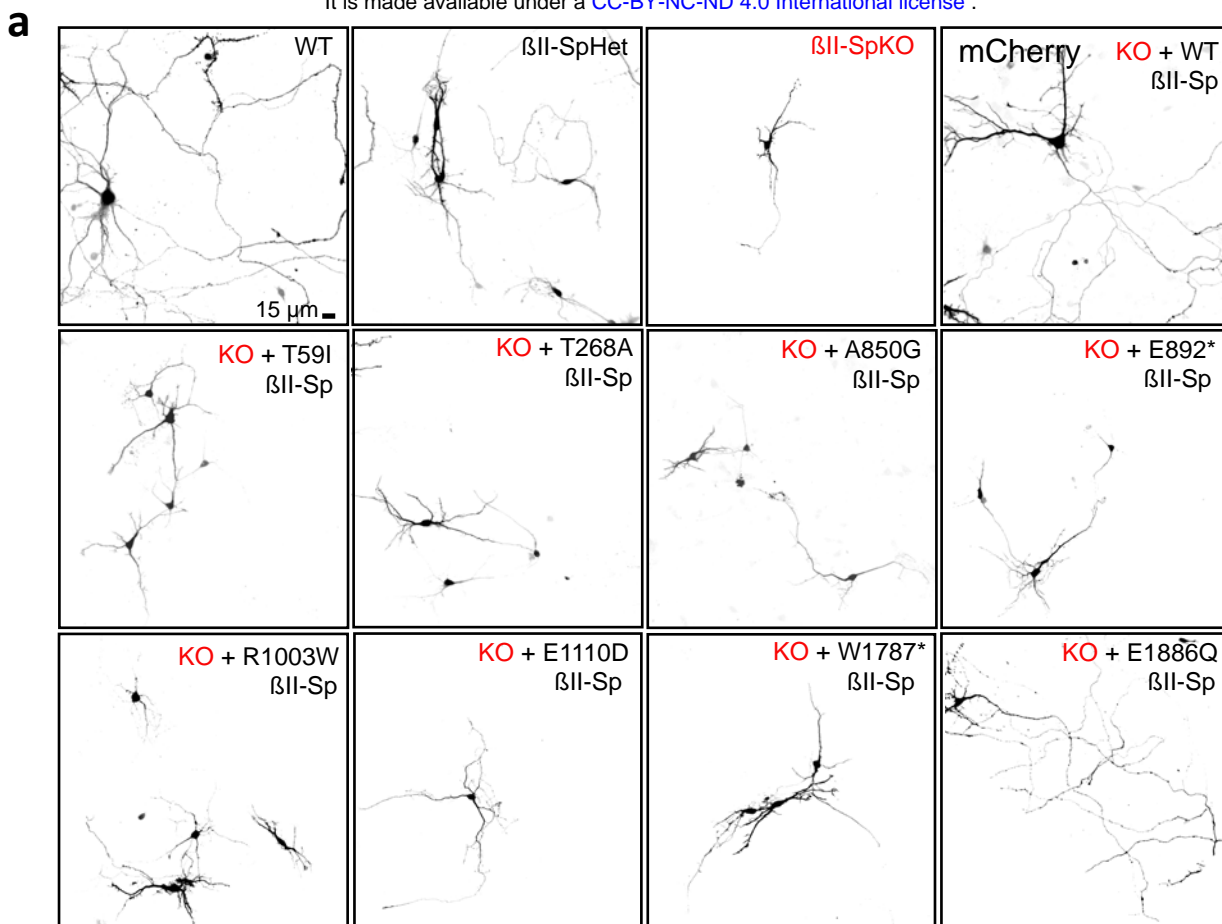


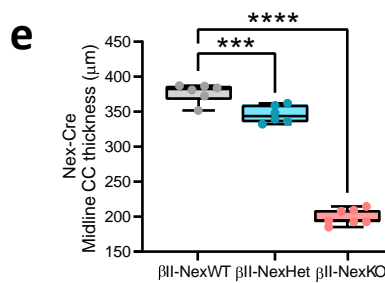
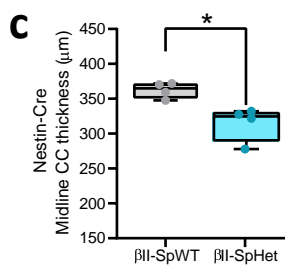
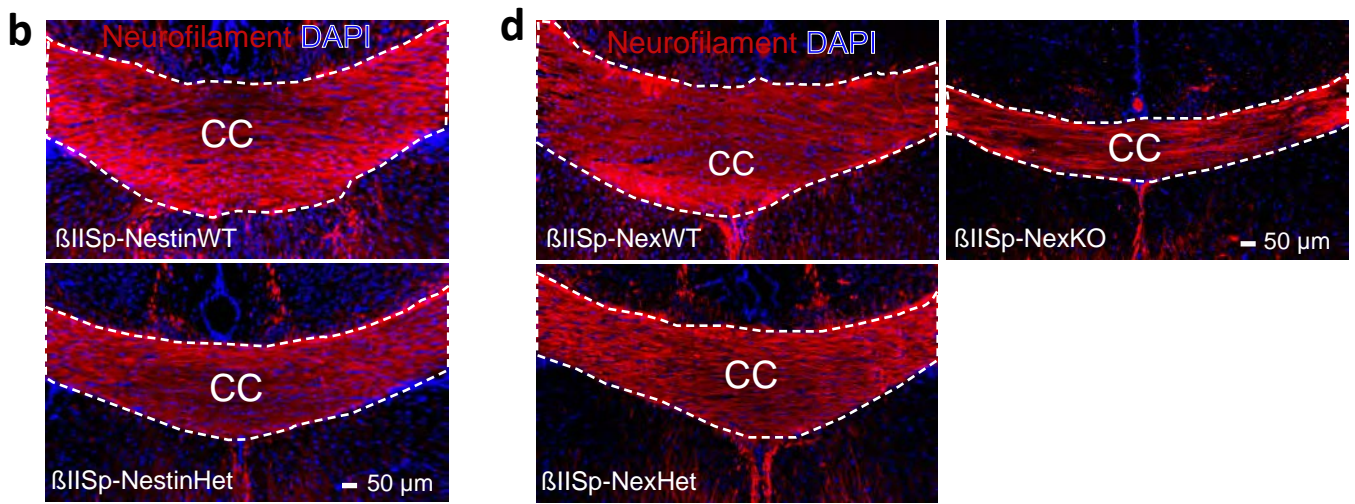
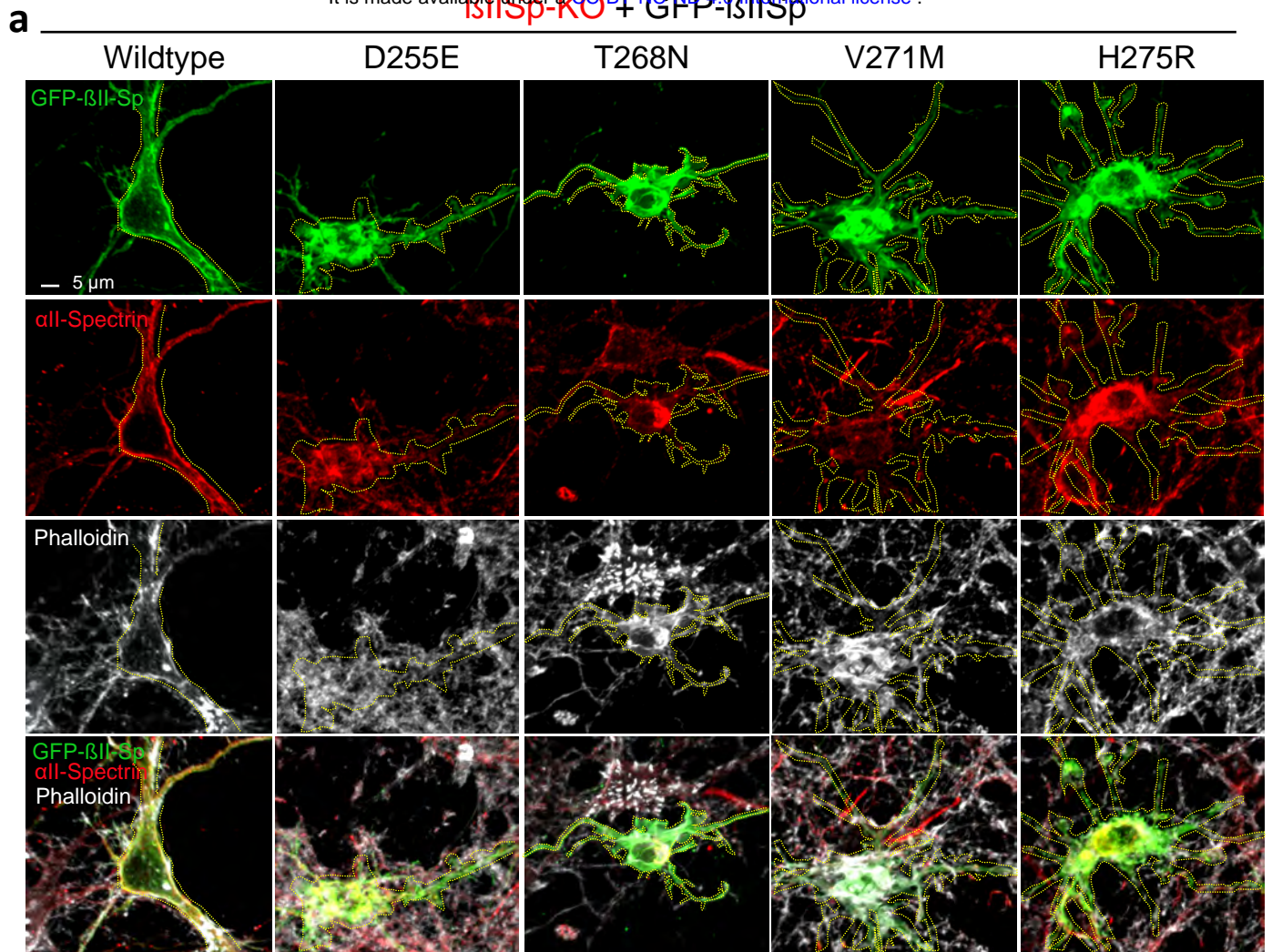




**i**

Closest CH1 - CH2 closed conformation interface residues		Mutation	Residues impacted by mutation	Predicted molecular consequences
<b>CH1</b>	<b>CH2</b>	<b>T59I</b>	L250	More hydrophobic side chain may increase CH2 binding
K62	D252	<b>G205D</b>	N233 & L234	Steric hindrance likely disrupts normal CH2 folding
<b>T59</b> , W63, W151, I154	<b>L250</b>	<b>G205S</b>		
L155	<b>T268</b>	<b>L247H</b>	Y273 & Y276	Steric hindrance likely disrupts normal CH2 folding
<b>I159</b>	<b>H275</b>	<b>L250R</b>	T59, W63, W151, & I154	Steric hindrance of large charged residue in hydrophobic CH1 pocket
		<b>D255E</b>	K62	Longer side chain may impair CH1 binding
		<b>T268A</b>	L155 & I159	Methyl group loss may impair hydrophobic interaction with CH1 residues
		<b>T268S</b>		Longer, more hydrophilic side chain may impair CH1 binding
		<b>T268N</b>		
		<b>V271M</b>	I159	Longer side chain may impair CH1 binding or new hydrophobic interaction may increase binding
		<b>H275R</b>	I159	Longer, charged basic side chain may impair CH1 binding and interact with acidic residue D51 on actin, enhancing binding





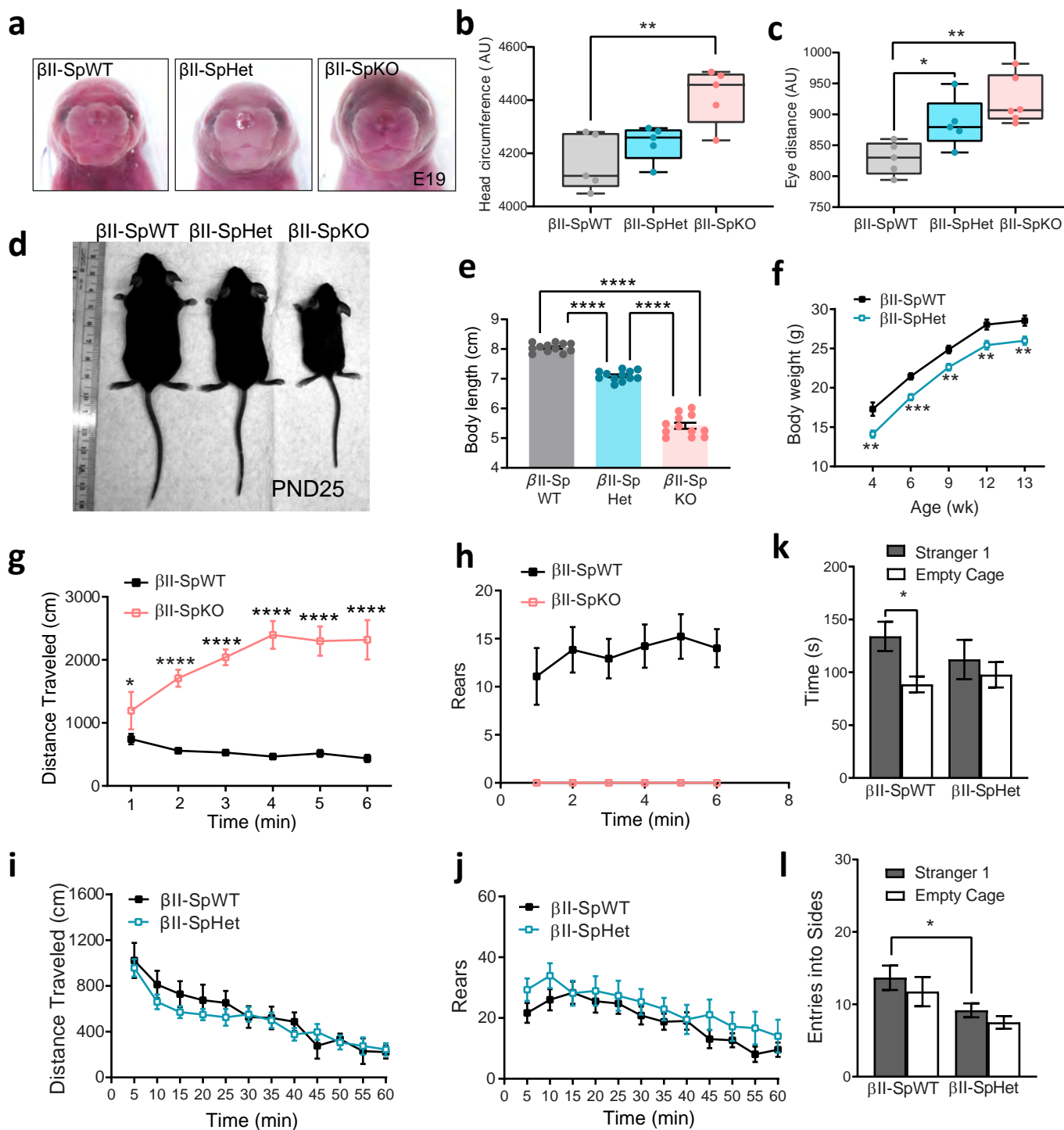


Table 1

Proband ID	P1	P2	P3	P4	P5	P6	P7	P8	P9	P10	P11	P12	P13	P14	P15	P16	P17	P18	P19	P20	P21**	P22**	P23	P24	P25	P26	P27	P28	P29		
Variant	p.T59I	c.475-1G>A p.(1159_Q160del)?	p.C183*	p.G205S	p.G205D	c.647+1G>T p.(V190_R216del)?	p.L247H	p.L250R	p.D255E	p.T268A†344L	p.T268N	p.T268S	p.V271M	p.H275R	p.R411W	p.R411Q	p.E491Q	p.A850G	p.E892*	p.R1003W	p.R1003W	p.R1003W	p.A1086T	p.E1110D	p.G1398S	p.S1674P	p.W1787*	p.E1886Q	c.5961+21>C p.(11988Afs*90)?	TOTAL	
Phenotype evaluation	C	C	-	P	C	P	C	C	C	C	C	C	C	C	C	C	C	C	C	C	C	C	C	C	P	C	C	C	C	C	
Age at last exam (y/m)	11m	13y	U	26y	6y 2m	NA	8y 9m	7y 8m	12y 5m	10y	6y 7m	11y	3y 7m	9y	6y	21m	3y 2m	7y	5y 10m	10y	15y	2y	5y 10m	U	9y	16y	3y 11m	18y			
Sex	Ma	Fe	Ma	Fe	Ma	Fe	Ma	Fe	Ma	Fe	Ma	Ma	Ma	Ma	Ma	Ma	Ma	Fe	Ma	Ma	Fe	Ma	Ma	Fe	Ma	Fe	Fe	Fe	Fe	17 male	
<b>Neurodevelopment</b>																															
Developmental Delay	+	+	U	+	+	+	+	+	+	+	+	+	+	+	+	+	+	+	+	+	+	+	+	+	U	+	+	-	+	26/27	
Speech Delay	+	S	U	+	+	U	+	+	S	+	+	+	+	+	+	+	+	+	+	+	+	+	+	Mi	+	U	+	+	-	-	24/26
Motor Delay	+	+	U	+	+	U	+	+	+	+	+	+	+	+	+	-	+	+	+	+	+	+	+	Mi	+	U	-	-	-	Mi	22/26
ID	Mo	S	U	Mi	Mi	U	+	S	S	S	U	S	Mi	Mo	Mo	U	U	M-S	L-N	M-M	Mo	+	-	-	U	Mi	Mi	M-S	-	20/23	
Regression	-	-	U	U	-	U	-	-	+	+	-	+	-	-	-	-	-	-	-	-	-	-	-	-	U	-	-	-	-	3/25	
<b>Other Neurological</b>																															
Epilepsy/seizure	+	U	U	U	+	U	-	NA	+	+	-	+	U	-	-	-	-	F	-	-	+	-	F	-	U	-	+	-	-	9/22	
EEG abnormalities	+	U	U	+	+	U	NA	NA	+	-	NA	+	U	-	-	NA	NA	-	NA	NA	+	-	NA	NA	U	-	NA	NA	-	6/13	
Abnormal brain MRI	+	+	U	U	-	U	-	NA	-	+	-	-	-	-	-	+	-	+	NA	NA	-	+	NA	NA	U	NA	-	+	NA	7/18	
Micro-/macrocephaly	↑	↓	U	U	-	U	-	-	↓	↓	↓	↑	↑	-	-	U	↑	U	U	-	-	-	-	U	↑	U	↓	NA	+	U	↓5, ↑5/19
Sleep disturbances	-	-	U	U	-	U	+	+	+	-	U	+	U	U	-	U	-	+	-	-	-	-	-	+	U	-	U	+	-	7/20	
<b>Behavior</b>																															
ASD/autistic features	ND	-	U	+	-	U	-	+	+	ND	-	-	U	U	-	U	-	-	+	-	-	-	-	+	U	-	-	+	-	6/21	
ADD/ADHD	U	U	U	+	-	U	+	+	-	ND	+	+	+	+	U	U	-	U	-	+	-	+	-	-	+	U	-	+	-	11/20	
Anxiety	U	U	U	+	-	U	-	-	-	ND	U	+	-	-	+	U	-	-	-	-	-	U	-	-	U	U	U	NA	-	3/17	
Obsessive behavior	U	U	U	+	-	U	-	-	-	ND	-	-	-	-	-	U	-	U	-	-	-	-	U	-	-	+	U	U	-	2/19	
Emotional lability*	U	U	U	U	-	U	-	+	-	U	-	-	+	+	-	U	-	-	-	+	-	+	-	+	U	U	+	-	-	7/20	
Aggressive behavior	U	U	U	U	-	U	-	+	-	U	+	+	-	-	+	U	-	-	-	U	U	U	-	+	U	U	+	-	-	6/17	
<b>Systemic problems</b>																															
Abnormal Movement	-	+	U	U	-	U	+	NA	+	+	-	-	-	+	+	-	-	-	-	-	-	-	-	-	U	U	-	-	+	7/23	
Hypo-/hypertonia	↓	↑	U	U	-	U	-	NA	↓	↑	-	-	-	-	↓	↓	↓	↑	-	-	↓	↓	-	-	U	U	U	↓	-	↑8, ↑4/22	
EMG abnormality	NA	NA	U	U	NA	U	NA	NA	NA	NA	+	NA	NA	NA	NA	NA	NA	NA	U	NA	NA	U	NA	NA	U	NA	NA	NA	-	1/2	
Hearing impairment	-	U	U	U	-	U	-	+	-	+	-	-	-	-	-	-	-	+	-	-	+	-	-	-	U	+	-	-	-	5/24	
Dysmorphology	+	+	U	+	-	U	+	+	+	NA	+	+	+	+	+	+	+	-	-	+	-	-	-	-	U	+	+	+	+	18/25	

Ma=male, Fe=female, P=partial, C=Complete, ID=intellectual disability, \*Emotional Liability includes tantrums and depression, Mi=mild, Mo=moderate, S=severe, M-M=mild to moderate, M-S=moderate to severe, L-N=low to normal, U=unknown, ND=not diagnosed, NA=not assessed, F=febrile seizures only, ↓= micro or hypo, ↑= macro or hyper, \*\*=half-siblings